Human iPSC-based neurodevelopmental models of globoid cell leukodystrophy uncover patient- and cell type-specific disease phenotypes

Elisabeth **Mangiameli**[1], Anna **Cecchele**[1], Francesco **Morena**[2], Francesca **Sanvito**[3], Vittoria **Matafora**[4], Lucrezia **Della Volpe**[1], Daniela **Gnani**[1], Marianna **Paulis**[5,6], Lucia **Susani**[5,6], Sabata **Martino**[2], Raffaella **Di Micco**[1], Angela **Bachi**[4], and Angela **Gritti**[1]

1. San Raffaele Telethon Institute for Gene Therapy (SR-Tiget), IRCCS San Raffaele Scientific Institute, Via Olgettina 60, 20132 Milan, Italy
2. Department of Chemistry, Biology and Biotechnology, University of Perugia, Via del Giochetto, 06123 Perugia, Italy
3. Pathology Unit, IRCCS San Raffaele Scientific Institute, Via Olgettina 60, 20132 Milan, Italy
4. IFOM-FIRC Institute of Molecular Oncology, Via Adamello 16, 20139 Milan, Italy
5. Humanitas Clinical and Research Center-IRCCS, Rozzano, Milan, Italy.
6. National Research Council (CNR)-IRGB/UOS of Milan, Milan, Italy.

Correspondence:

Angela Gritti, San Raffaele Telethon Institute for Gene Therapy (SR-Tiget), IRCCS San Raffaele Scientific Institute, Via Olgettina 60, 20132 Milan, Italy; e-mail: gritti.angela@hsr.it

Summary

Globoid Cell Leukodystrophy (GLD, or Krabbe disease) is a rare lysosomal storage disease caused by inherited deficiency of β-galactocerebrosidase (GALC). The build-up of psychosine and other undegraded galactosylsphingolipids in the nervous system causes serious demyelination and neurodegeneration. The molecular mechanisms of GLD are poorly elucidated in neural cells and whether murine systems faithfully recapitulate critical aspects of the human disease is still to be defined.

Here, we established a collection of GLD patient-specific induced pluripotent stem cell (iPSC) lines. We differentiated iPSCs from two patients – bearing different disease-causing mutations - into neural progenitors cells (NPCs) and their neuronal/glial progeny, assessing the impact of GALC deficiency and lentiviral vector-mediated GALC rescue/overexpression by means of phenotypic, biochemical, molecular, and lipidomic analysis. We show a progressive increase of psychosine during the differentiation of GLD NPCs to neurons and glia. We report an early and persistent impairment of glial and neuronal differentiation in GLD cultures, with peculiar differences observed in the two GLD lines. GLD cells display a global unbalance of lipid composition during the iPSC to neural differentiation and early activation of cellular senescence, depending on the disease-causing mutation. Restoration of GALC activity normalizes the primary pathological hallmarks and partially rescues the differentiation program of GLD NPCs.

Our results show that multiple mechanisms besides psychosine toxicity concur to CNS pathology in GLD and highlight the need of a timely regulated GALC expression for proper lineage commitment and differentiation of human NPCs. These findings have important implications for establishing tailored cell/gene therapy strategies to enhance disease correction in GLD.

Keywords

Pluripotent stem cells, leukodystrophy, Krabbe disease, gene therapy, neural progenitors, oligodendrocytes, senescence.

Running title

Human iPSC-based models of GLD

50 **Introduction**

51 Globoid Cell Leukodystrophy (GLD, or Krabbe disease) is a rare lysosomal storage disorder (LSD)
52 caused by inherited deficiency of β-galactocerebrosidase (GALC), a key enzyme in the catabolism of
53 galactosphingolipids, e.g. galactosylceramide and galactosylsphingosine (psychosine) (Suzuki and Suzuki,
54 1970). The infantile forms are characterized by relentless demyelination and neurodegeneration of the
55 central and peripheral nervous system (CNS, PNS). Allogeneic hematopoietic stem/progenitor cell (HSPC)
56 transplant - the only therapeutic option for GLD patients - provides a functional GALC enzyme to the
57 affected organs through the engraftment of HSPC-derived myeloid progeny. However, it fails to fully
58 correct the severe CNS pathology, even if performed at the asymptomatic stage (Allewelt et al., 2016),
59 likely because of the insufficient GALC supply provided by HSPC-derived microglia in the brain. *In vivo*
60 and *ex vivo* gene therapy (GT) approaches using lentiviral vectors (LV) and adeno-associated vectors
61 (AAV) benefit GLD animal models (Bradbury et al., 2018; Gentner et al., 2010; Lattanzi et al., 2010, 2014;
62 Lin et al., 2005; Meneghini et al., 2016; Rafi et al., 2015; Ricca et al., 2015; Ungari et al., 2015). The
63 advantage of *ex vivo* GT with LV-modified HSPCs in infants affected by metachromatic leukodystrophy
64 (MLD) – a similar LSD (Biffi et al., 2013; Sessa et al., 2016), suggests that a similar approach might be
65 translated to GLD. Still, the obstacles in reaching safe, widespread and stable expression of therapeutic
66 GALC levels in the human CNS still limits the clinical development of these GT strategies to GLD.

67 Studies in GLD animal models suggest that a modest accumulation of psychosine in brain tissues
68 impairs CNS and PNS development from neural progenitor cells (NPCs) (Castelvetri et al., 2011;
69 Santambrogio et al., 2012; Teixeira et al., 2014). Psychosine storage is present in nervous tissues before
70 the onset of symptoms, even if high levels are required to trigger overt cytotoxicity, likely with cell- and
71 tissue-specific sensitivity. Besides the effects exerted on myelin and axons, psychosine – and other
72 substrates in the GALC-related sphingolipid pathway (Hannun and Obeid, 2017) - directly or indirectly
73 affect glial and neuronal cell homeostasis interfering with lipid content and distribution (Giri et al., 2006;
74 White et al., 2009), altering proteostasis network (Pellegrini et al., 2019), promoting apoptosis (Jatana et
75 al., 2002), lysosomal dysfunction (Folts et al., 2016; Samie and Xu, 2014), and autophagy (Del Grosso et
76 al., 2019). Growing evidence points to a previous underestimated association between lysosomal
77 dysfunction, protein misfolding/aggregation, lipid unbalance, and senescence in multiple organisms and
78 cell types (Buratta et al., 2017; Irahara-Miyana et al., 2018; Lee et al., 2014; Lizardo et al., 2017; Smith et
79 al., 2014; Trayssac et al., 2018). Also, recent observations implicate NPCs and oligodendroglial progenitor
80 cells (OPCs) senescence in the pathogenesis of neurodegenerative disorders with protein aggregation
81 (Zhang et al., 2019) and neuroinflammatory demyelinating disorders (Nicaise et al., 2019), providing a

strong rationale for investigating the potential implication of these processes in GLD. Altogether, these complex and still poorly elucidated events may contribute to the multifaceted aspects of GLD pathology and explain the modest efficacy of conventional or experimental therapies in correcting CNS and PNS pathology in GLD animal models and patients (Allewelt et al., 2016; Hawkins-Salsbury et al., 2015; Rafi et al., 2015; Ricca et al., 2015).

More than 100 disease-causing mutations in the human *GALC* gene have been described (Wenger and Luzi, 2014), among which a 30-kb deletion accounts for 40% of pathogenic alleles in the Caucasian population (Rafi et al., 1995). The occurrence of this large gene deletion in homozygosis is associated to the early-onset and most severe disease forms. The genotype-phenotype correlation is less clear for the many missense/nonsense mutations occurring in homozygosis or compound heterozygosis, which may be associated to variable residual GALC activity and severe to mild disease variants (Duffner et al., 2011, 2012; De Gasperi et al., 1996, 1999; Jalal et al., 2012; Tappino et al., 2010). Misfolded GALC proteins evoke different Unfolded Protein Response (UPR) activation (Irahara-Miyana et al., 2018) and show mutation-specific alteration of trafficking to lysosomes and processing (Shin et al., 2016), suggesting the occurrence of pathological cascades that are independent from or act in synergy with primary lipid storage in determining the complex GLD phenotype. Thus, studying the mechanisms linking the primary mutation-specific event(s) to progressive cell dysfunction and death is relevant and requires appropriate experimental models.

Murine, canine and non-human primate models of GLD (Wenger, 2000) are valuable to test the safety and efficacy of novel therapies; nevertheless, they fail to fully recapitulate the spectrum of pathological manifestations observed in patients. Also, the most used mouse model (Suzuki, 1983) and non-human primate model of GLD (Borda et al., 2008; Luzi et al., 1997) carry spontaneous mutations that are not found in humans. Currently used GLD human cellular models include patient-specific fibroblasts (Berardi et al., 2014; Gama Sosa et al., 1996; Rafi et al., 1996; Ribbens et al., 2013; Spratley et al., 2016), human hematopoietic cells (Martino et al., 2009), or epithelial cell lines with induced GALC mutations (Lee et al., 2010; Shin et al., 2016) that hardly resemble the metabolic and functional features of NPCs and their differentiated progeny. Thus, there is a strong need for human-derived experimental models to explore GLD pathogenesis and test correction strategies.

Human induced pluripotent stem cells (iPSCs) (Yamanaka, 2007) offer a unique tool to analyze the molecular consequences of pathogenic mutations in the context of the genetic background of individual patients. The differentiation of iPSCs in neural cells has boosted CNS disease modelling and therapeutic screening (Shi et al., 2017). Human iPSCs are available from a variety of LSDs (Huang et al.,

114 2012) but there are no reports describing GLD-derived iPSCs.

115 Here, we established GLD patient-specific iPSC lines as a reliable human model for elucidating
116 GLD pathogenesis and testing the biological efficacy of gene therapy strategies in relevant neural cell
117 types. To this end, we differentiated iPSCs into NPCs and progeny (oligodendrocytes, neurons, and
118 astrocytes), and monitored the appearance/progression of cell type- and patient-specific primary and
119 secondary defects in GLD cells. Finally, we assessed the impact of GALC reconstitution/overexpression
120 (achieved by lentiviral-mediated gene transfer) in reverting the pathological phenotype and its potential
121 impact on the biology of human NPCs and progeny.

122

123 **Results**

124

125 **GLD iPSCs show undetectable GALC activity and psychosine storage but display normal pluripotency**
126 **features**

127 We generated iPSCs from fibroblasts of 5 GLD patients with distinct biallelic mutations in the
128 *GALC* gene (homozygous or compound heterozygous) resulting in the infantile form of the disease.
129 Control iPSC lines were generated from fibroblasts of two unrelated normal donors (ND1, adult; ND2,
130 neonatal) and one non-affected relative (ND3, parent of GLD1)(**Table S1**). GALC activity in ND fibroblasts
131 was 2.42 nmol*h/mg (ND1), 3.89 nmol*h/mg (ND2), and 1.56 nmol*h/mg (ND3), while it was below the
132 limit of detection in all GLD fibroblasts, indicating that the mutated GALC proteins have no residual
133 functionality. By using an integration-free, feeder-free microfluidic reprogramming system (Luni et al.,
134 2016) we obtained several iPSC clones from each patient and ND fibroblast line (reprogramming
135 efficiency: 2-53%)(**Figure S1A**). After 6-10 subculturing passages, we randomly selected two clones/line
136 for further analysis (**Figure S1A**). The presence of specific GALC mutations was verified by PCR analysis
137 and sequencing (**Figure S1B-C**).

138 We assessed the pluripotency of GLD and ND iPSC clones by performing standard assays,
139 including RT-PCR **(Figure S1D**) and immunocytochemistry (**Figure 1A**) for the markers NANOG, SOX2,
140 KLF4, OCT4, and TRA1-60. Analysis of endodermal-, mesodermal-, and ectodermal-specific markers in
141 embryoid bodies (**Figure 1B; Figure S1E**) and histological assessment of teratomas (**Figure S1F**)
142 confirmed the ability of GLD and ND iPSCs to differentiate in multiple cell types and tissues both *in vitro*
143 and *in vivo*.

144 All the GLD iPSC clones displayed undetectable GALC activity (**Figure 1C**) and significant
145 psychosine storage (50-100-fold the ND levels), which was not observed in the parental fibroblasts

146 (**Figure 1D).**

147 Overall, GLD patient iPSCs showed the primary biochemical GLD hallmarks but expressed normal
148 stem cell properties, justifying their use as human-based GLD model.

149

150 **LV-mediated gene transfer in GLD iPSCs rescues GALC activity and normalizes psychosine storage**

151 We focused on the mutant lines GLD1 and GLD5 (two clones/line) for further characterization
152 and gene transfer studies. GLD1 is homozygous for the large 30 Kb *GALC* gene deletion
153 (c.1161+6532_polyA+9kbdel) responsible for the production of a truncated protein lacking the whole
154 coding region for the 30kDa subunit and 15% of the coding region for the 50kDa subunit (Luzi et al.,
155 1995; Tappino et al., 2010). GLD5 is homozygous for a missense mutation (c.1657G>A) that is predicted
156 to cause GALC protein misfolding (De Gasperi et al., 1996; Tappino et al., 2010). ND1 and ND2 iPSCs (two
157 clones/lines) were used as controls for all the subsequent experiments (**Table S1 and Figure S1A**).

158 We selected ND and GLD iPSC clones with normal karyotype (**Figure S2**) and used these cells
159 within subculturing passages 8-30. To restore GALC activity, we transduced GLD1 and GLD5 iPSC clones
160 using a laboratory grade/scale VSV-pseudotyped third-generation lentiviral vector (LV) encoding for the
161 human (h) *GALC* gene tagged with the Myc peptide under the control of the human phosphoglycerate
162 kinase (PGK) promoter (LV.hGALC) (Meneghini et al., 2016)(**Figure 2A**). Pilot dose-response experiments
163 showed the proficient transduction of iPSC clones at Multiplicity of Infection (MOI)=2 (**Figure S3A**), which
164 was selected to transduce GLD1.1, GLD1.3, GLD5.2, GLD5.6 and ND2.2 iPSC clones in all the following
165 experiments. LV.hGALC-transduced GLD (GLD^{GALC}) and ND (ND^{GALC}) iPSCs showed variable vector copy
166 number (VCN) (**Figure 2B**), upregulation of GALC mRNA (**Figure 2C**), efficient transgene expression
167 (**Figure 2D-E),** and increase in enzymatic activity (reaching supraphysiological levels; **Figure 2F**). We
168 observed a clear correlation between VCN, GALC mRNA expression and enzymatic activity (**Figure S2B**).

169 The transgenic GALC enzyme was functional, as shown by the normalization of psychosine levels
170 in GLD iPSCs (**Figure 2G**), which do not show other pathological hallmarks related to GALC deficiency (i.e.
171 GalCer accumulation, increased LAMP1 expression – index of lysosomal expansion) (**Figure S3C-D).**
172 Importantly, LV transduction and GALC overexpression did not affect the pluripotency (**Figure S3E**) and
173 proliferation rate (**Figure S3F**) of ND and GLD iPSC clones.

174

175 **GLD and ND iPSC-derived NPCs are generated with similar efficiency and display comparable**
176 **phenotype**

177 We next assessed the impact of GALC deficiency and LV-mediated GALC restoration in iPSC-

178 derived neural cells. We differentiated GLD, GLD^{GALC}, ND, and ND^{GALC} iPSCs into NPCs using a published
179 protocol (Chambers et al., 2009)(**Figure 3A**). At the end of the differentiation, iPSC-NPCs showed
180 downregulation of pluripotency markers (OCT4, NANOG) and upregulation of NPC markers (NESTIN,
181 PAX6, FOXG1), early neuronal (Doublecortin, DCX) and glial cell (ASCL1) markers **(Figure 3B-C).** We
182 obtained NPCs with similar efficiency from untransduced (UT) and LV.hGALC-transduced GLD and ND
183 iPSCs in multiple rounds of differentiation experiments with the only exception of clone GLD1.3^{GALC},
184 which consistently displayed abnormal morphology (not shown) and modest PAX6 upregulation as
185 compared to other clones (**Figure 3B**). Based on these observations suggesting incomplete/defective
186 neural induction, we excluded clone GLD1.3^{GALC} from further analysis. All the selected NPC lines stably
187 expanded in culture for 5-6 passages in the presence of neural medium (N2) supplemented with EGF,
188 bFGF and Rock inhibitor (**Figure 3D).** Thus, ND and GLD iPSC-derived NPCs display bona-fide NPC
189 molecular and phenotypic features.
190
191 **Time- and cell type-dependent transcriptional regulation of GALC expression and activity during iPSC-**
192 **NPC differentiation to neurons and glia**
193 Myelinating cells and neurons are highly susceptible to psychosine-mediated toxicity, but
194 astrocytes are also affected (Misslin et al., 2017; Potter and Petryniak, 2016). Therefore, we envisaged
195 that differentiation of iPSC-NPCs into mixed neuronal/glial cultures would better model the composite
196 GLD pathology. We adapted a published protocol (Frati et al., 2018) to generate cell populations
197 containing neurons, astrocytes, and oligodendrocytes from ND, GLD, GLD^{GALC}, and ND^{GALC} iPSC-NPCs.
198 Cultures were evaluated at day 0 (d0; NPCs), d7, d14, and d24 of differentiation (**Figure 3E**), to track the
199 time-course GALC expression/activity and the glial/neuronal cell commitment and maturation by means
200 of biochemical and molecular analysis.
201 The GALC transcript was expressed at low levels in both ND and GLD iPSC clones (GLD1 and GLD5
202 mutations are not predicted to impact on mRNA transcription) and was upregulated during the neural
203 induction and neuronal/glial differentiation (**Figure 3F**). GALC mRNA expression in GLD^{GALC} and ND^{GALC}
204 iPSCs was constant over time, due to the high and stable expression driven by the constitutive PGK
205 promoter **(Figure 3F).**
206 GALC enzymatic activity moderately increased in ND differentiated cultures (d14 and d24) as
207 compared to the iPSCs and NPCs counterpart (≈1.5 fold) **(Figure 3G).** The GALC activity in GLD^{GALC} cultures
208 progressively decreased during the iPSC to neural differentiation to reach physiological levels at d14 and
209 d24, whereas ND^{GALC} differentiated cultures maintained supraphysiological GALC activity (≈3-fold the ND

210 counterpart at d14 and d24). (**Figure 3H**). The stable VCN measured in ND^{GALC} and GLD^{GALC} cultures at
211 different time points of differentiation (**Figure 3H**) rules out the possibility that the decrease in
212 enzymatic activity results from the counter selection of cells harboring high VCN over time.
213 Overall these data show that LV-mediated gene transfer ensures (supra)physiological GALC
214 expression and activity in iPSC-NPCs and neuronal/glial progeny, and highlight a stringent time- and cell
215 type-dependent transcriptional regulation of GALC activity during NPCs maturation.
216
217 **GLD iPSC-NPCs display defective neural and glial differentiation: impact of GALC**
218 **rescue/overexpression on psychosine levels and phenotype.**
219 Commitment of NPCs to oligodendrocyte precursors (OPCs) and differentiation in mature
220 oligodendrocytes (OL) is driven by the timely regulated expression of oligodendroglial genes. GLD cells
221 displayed an altered pattern of expression of several oligodendroglial master genes (NKX2.2, OLIG2,
222 SOX10, PDGFRα, MBP) as compared to ND cells, with some differences between GLD1 and GLD5 (e.g.
223 sustained expression of PDGFRα along the differentiation and increased SOX10 expression in
224 differentiated GLD5 cells) **(Figure S4A).** These data suggest an altered oligodendroglial differentiation
225 program, which is only partially normalized in GLD^{GALC} cultures. Interestingly, a similar alteration is also
226 observed ND^{GALC} cultures (**Figure S4A**). Immunofluorescence and WB analysis confirmed an early and
227 persistent reduction of oligodendroglial cells (OLIG2+, APC+ cells; **Figure 4A-B)** and a significant
228 downreguation of OLIG1 protein expression (**Figure S4B**; d24) in both GLD1 and GLD5 NPC-derived
229 cultures as compared to the ND counterpart, highlighting a partial phenotypic rescue in GLD^{GALC} cells and
230 a detrimental impact of GALC overexpression in ND cultures (**Figure 4A-B** and **Figure S4B).**
231 GALC deficiency affected neuronal differentiation, with some differences observed in the two
232 GLD lines. Real-time PCR analysis revealed similar expression of the neuronal master transcription factor
233 NeuroD1 in ND and GLD lines. In contrast, doublecortin (DCX) expression was reduced in GLD5 as
234 compared to GLD1 and ND differentiated cells **(Figure S5A).** In line with these results, GLD5 cultures
235 showed a significant time-dependent reduction of TUJ1+ neurons (**Figure 4C-D**) and a decreased and/or
236 delayed TUJ1 and neurofilament (NF)-M protein expression, respectively (**Figure S5B-C).** The major
237 decrease in the expression of acetylated and polyglutamated tubulin and phosphorylated neurofilaments
238 observed in GLD5 cultures (d14 and d24) further suggested an important neuronal loss and/or defective
239 neuronal differentiation/maturation (**Figure S6**). In contrast, GLD1 cultures displayed a normal
240 proportion of neuronal cells (**Figure 4C-D)** and normal kinetic of expression of neuronal proteins (**Figure**
241 **S5B-C)**. The quantitative and qualitative neuronal defects observed in GLD5 cultures were rescued in

242 differentiated GLD^{GALC} cultures (**Figure 4C, Fig S5B-C**), which also showed an early upregulation of NF-M
243 protein as compared to the ND cultures and untransduced counterparts (**Figure S5C),** suggesting an
244 accelerated neuronal differentiation associated to GALC overexpression.

245 GFAP+ astroglia is the less represented and most variable cell population in our differentiated
246 cultures (<10% in ND cultures at day 24). Nevertheless, RT-PCR (**Figure S7A**), IF (**Figure 4C-D**) and WB
247 analysis (**Figure S7B**) showed defective glial differentiation in GLD1 cultures, which virtually failed to
248 generate GFAP+ astrocytes. This defect was not rescued in GLD1^{GALC} cultures (**Figure 4C-D** and **Figure S7**).
249 In contrast, GLD5 and GLD5^{GALC} cultures showed normal percentages of GFAP+ cells and physiological
250 GFAP protein expression (**Figure 4C-D** and **Figure S7**). Similarly to what observed in oligodendrocytes,
251 GALC overexpression negatively affected the pattern of gene expression (**Figure S5, S6, S7**), the number
252 and morphology of ND neurons (**Figure 4C-D**, **Figure S5)** and astrocytes **(Figure 4C-D, Figure S7**),
253 particularly at the latest time point in culture. Finally, both GALC deficiency (GLD cultures) and forced
254 GALC expression (GLD^{GALC} and ND^{GALC} cultures) were associated to higher percentages of cells that
255 stained negative for the selected lineage-specific markers **(Figure S7C).**

256 Psychosine levels were low in GLD iPSC-NPCs and increased during differentiation, to reach ≈8
257 (GLD1) and ≈30 fold (GLD5) the normal levels at d24 (**Figure 5A**). The psychosine build up was not
258 associated to a significant increase of cleaved caspase 3+ cells (**Figure 5B**) or to enhanced phospholipase
259 A2 (PLA2) activity (**Figure 5C**), which has been associated to psychosine-induced apoptotic cell death
260 (Misslin et al., 2017). Psychosine levels were normalized in GLD1^{GALC} cultures and strongly reduced in
261 GLD5^{GALC} cultures (≈2-fold the normal), in line with the enzymatic reconstitution. We observed moderate
262 enlargement of lysosomal vesicles (Lysotracker assay) (**Figure 5D**) in GLD NPCs (GLD1>GLD5) and
263 increased LAMP1 protein expression in GLD and ND^{GALC} differentiated cultures (**Figure 5E**).

264 Taken together, these data show that: i) GALC deficiency severely impairs the differentiation of
265 hiPSC-derived NPCs into oligodendrocytes, neurons, and astrocytes, with cell type- and patient-specific
266 phenotypes; ii) LV-mediated GALC reconstitution in GLD cells reduces psychosine levels and provides
267 partial phenotypic rescue in GLD neural progeny; iii) GALC-overexpressing ND cells display lysosomal
268 expansion and a defective neuronal and glial phenotype, suggesting that a tight regulation of GALC
269 expression is required to ensure proper NPC functionality and preserve multipotency**.**

270

271 **Early activation of a senescence response in GLD5 iPSC-derived neural cells**

272 Our data suggested a marginal contribution of cell death to the loss of GLD neurons and glial
273 cells. Therefore, we explored whether the altered differentiation programs of GLD NPCs and progeny

274 could be caused by an alteration of proliferative potential. By performing and quantifying Ki67/nestin
275 immunostaining at the different stages of the differentiation protocol, we showed a time-dependent
276 decrease in the percentage of proliferating cells in all ND and GLD cultures, indicating the lineage
277 commitment of iPSC-NPCs, their exit of cell cycle and acquisition of a post-mitotic state (**Figure 6A).**
278 Interestingly, EdU incorporation assay performed at the same time points during differentiation
279 showed an earlier and more drastic drop in the percentage of cells in active S-phase in GLD5 cultures
280 as compared to ND and GLD1 counterparts (**Figure 6B).** This proliferation drop was recovered in
281 $GLD5^{GALC}$ cultures (**Figure 6B**).

282 We next investigated whether the early proliferation arrest highlighted in GLD5 cultures was
283 associated with the establishment of cellular senescence, a biological process characterized by stable
284 growth arrest, accumulation of DNA damage and activation of a pro-inflammatory program
285 collectively known as SASP, senescence-associated secretory phenotype (He and Sharpless, 2017). We
286 detected upregulation, at the transcript and protein levels, of the cell cycle inhibitor p21 (**Figure 6C-**
287 **D)** and increased nuclear levels of DNA damage response (DDR) markers 53BP1 (**Figure 6E)** and yH2AX
288 **(Figure S8A-B)** as early as d7 post-differentiation. The induction of DDR and p21 was specific of GLD5
289 cultures, not reported in ND or GLD1 cultures, and was partially rescued by in $GLD5^{GALC}$ cultures. We
290 also observed a dramatic increase in the percentage of Senescence Associated (SA) β-gal positive cells
291 in GLD5 (but not ND or GLD1 cultures) with a peak at d7 of differentiation (**Figure 6F**), induction of
292 the senescence-associated marker p16 (**Figure S8C**), and of the SASP pro-inflammatory factors TNF-α
293 and IL1-β (**Figure S8D-E**). These senescence-associated hallmarks were reduced in $GLD5^{GALC}$ cultures.

294 Altogether, our data suggest that GLD5 iPSC-derived NPCs activate an early senescence
295 program that hampers physiological lineage commitment/differentiation. This senescent phenotype
296 is patient-specific (as it is not evident in GLD1 cells), and is rescued by supplying physiological levels
297 of a functional GALC enzyme.

298

299 **GLD cells display an altered lipidomic profile during the iPSC to neural differentiation**

300 Sphingolipids display widespread developmental, physiological and pathological actions in the
301 CNS, and induce biological effects on various stem/progenitor cell types (Hannun and Obeid, 2017).
302 Given the central role of GALC in the sphingolipid metabolism, we performed an untargeted global
303 lipidomic profiling in ND, GLD, and GLD^{GALC} iPSCs, NPCs and neuronal/glial cell progeny (d14 of
304 differentiation) to elucidate the impact of GALC absence or enhanced expression during the iPSCs to
305 neural differentiation. Lipid extracts were normalized based on protein concentration and analyzed by

306 LC-MS-based lipidomics workflow. We determined the lipid species showing reproducible changes in two
307 independent profiling experiments with two biological replicates for each experiment.

308 We identified more than 800 lipid species, with a distinct signature and enrichment of specific
309 lipid classes in iPSCs (e.g. triacylglycerols, TAG; lyso-phosphatidylserine, LPS), NPCs (e.g.
310 phosphatidylcholine, PC), and differentiated progeny (e.g phosphatidylethanolamine, PE; sphingomyelin,
311 SM) (**Figure 7A**). We observed profound changes in a number of phospholipid classes in GLD as
312 compared to ND cells (i.e. TAG; Diacylglycerols, DAG; Monoacylglycerols, MAG; PC; PE;
313 Lysophosphatidylethanolamine, LPE; PS; SM; Ceramides, Cer; HexosylCeramides, HexCer)(**Figure 7B**).
314 Within the same lipid class, we detected differences related to the stage of differentiation (iPSCs vs.
315 NPCs. vs differentiated cells) and genotype (ND vs. GLD1 vs. GLD5). GLD1 and ND iPSCs often showed a
316 comparable abundance of all these lipid classes, while GLD5 iPSCs displayed a clearly different trend
317 (**Figure 7B**). The most striking differences between GLD1 and ND cells were observed in NPCs, which
318 showed decreased levels of PE/LPE and increased Cer and DAG levels. The different lipidomic profile
319 displayed by GLD1 and GLD5 cells become more evident as cells undergo differentiation. Indeed, when
320 compared to GLD1 and ND cells, GLD5 cells showed reduced PC, PE, HexCer, and SM, and a strong
321 accumulation of DAG, TAG, Cer, and PS **(Figure 7B**). The inverse pattern of Cer and SM expression in
322 GLD5 cell populations - and particularly in differentiated cells - suggests that excess Cer could result from
323 the SM-based synthetic pathway in these cells (Young et al., 2012).

324 LV-mediated rescue of GALC activity partially normalized the lipidomic profiles of GLD1 and GLD5,
325 as shown by the PCA analysis (**Figure 7C)** and lipid signature **(Figure S9A-B).** In GLD1^{GALC} cells we
326 observed a rescue of PC, PE, HexCer (iPSCs) and TAG (NPCs). In GLD5 ^{GALC} cells we observed the
327 normalization of HexCer and SM level, as well as a rescue to normal levels of all DAG, TAG and PC that
328 were mostly affected in GLD5 differentiated cells. LV-mediated GALC overexpression resulted in a
329 profound and global impact on the lipidome of ND cells. Coherently with the presence of supranormal
330 GALC activity, we detected in ND^{GALC} iPSCs, NPCs, and differentiated cells decreased levels of HexCer and
331 variable increase of Cer, but also of DAG and PS in comparison to ND counterparts (**Figure S9C**)**.**

332

333 **Discussion**

334 Human iPSCs have been differentiated into neurons and/or glial cells to model the neural defects
335 associated to several lysosomal storage diseases (LSDs) including mucopolysaccharidosis (Bayó-Puxan et
336 al., 2018; Canals et al., 2015; Kobolák et al., 2019; Lemonnier et al., 2011; Vallejo-Diez et al., 2018),
337 Niemann−Pick type C (Maetzel et al., 2014; Ordoñez and Steele, 2016; Trilck et al., 2013; Yu et al., 2014),

338 Pompe disease (Higuchi et al., 2014), Gaucher disease (Panicker et al., 2012; Sun et al., 2015; Tiscornia et
339 al., 2013), GM1 and GM2 gangliosidosis (Son et al., 2015)(Allende et al., 2018), NCL (Lojewski et al., 2014),
340 and MLD (Frati et al., 2018; Meneghini et al., 2017). To date, this is the first report describing a human
341 iPSC-based neural model of GLD.

342 The five GLD patient-derived fibroblast cell lines that we used for somatic cell reprogramming
343 have different mutations in the *GALC* gene, all of them associated to the infantile form of the disease. All
344 the selected GLD iPSC lines displayed normal phenotypic and functional properties despite having
345 undetectable GALC enzymatic activity and significant psychosine storage. The dispensability of lysosomal
346 enzymatic activity for somatic cell reprogramming and iPSC maintenance as well as the tolerability to
347 lipid storage has been described in human iPSCs in other LSD models (Canals et al., 2015; Lojewski et al.,
348 2014; Meneghini et al., 2017; Trilck et al., 2013). The LV-mediated supply of physiological or slightly
349 supraphysiological GALC activity (3-4 fold the ND levels) in GLD iPSCs normalizes psychosine levels,
350 confirming the potential of gene transfer to correct the primary storage in GALC-deficient human cells. In
351 line with our previous study (Meneghini et al., 2017), we did not experience LV-mediated toxicity in
352 hiPSCs, which were viable and functional for several passages after transduction, maintaining
353 pluripotency and stable GALC activity.

354 The GALC enzyme contributes to preserve NPCs functionality during post-natal murine CNS
355 development (Santambrogio et al., 2012), but this aspect was never investigated in human NPCs,
356 neurons, and glial cells. GLD iPSC-derived NPCs had levels of psychosine similar to their ND counterparts,
357 differently from the parental GLD fibroblasts and iPSCs, in which psychosine is elevated. Interestingly,
358 the lack of psychosine storage distinguishes human from murine NPCs (Santambrogio et al., 2012). The
359 differentiation of GLD iPSC-NPCs into oligodendrocytes, neurons, and astrocytes exacerbates the
360 pathological phenotype, in line with the relevant role of GALC during glial and neuronal differentiation
361 (Graziano and Cardile, 2015). Specifically, we observed an early and persistent loss of oligodendroglial
362 cells in both GLD1 and GLD5 NPC-derived cultures. GLD5 cultures also displayed a dramatic loss of
363 neurons, while astrocytes were less affected. We observed an opposite situation in GLD1 cultures, in
364 which neurons were normally generated while astrocytes were virtually lost.

365 The oligodendroglial and neuronal cell dysfunction/loss described in GLD murine models has
366 been associated to psychosine-mediated toxicity (Hawkins-Salsbury et al., 2013; White et al.,
367 2011)(Bongarzone et al., 2016; Ricca and Gritti, 2016). Importantly, even a modest psychosine storage
368 may affect neuronal and glial differentiation (Castelvetri et al., 2011; Santambrogio et al., 2012; Teixeira
369 et al., 2014). Increased psychosine levels have been detected in the brain of GLD human foetuses (Igisu

370 and Suzuki, 1984) and elevated psychosine blood concentration is considered a specific marker in
371 infantile GLD patients (Escolar et al., 2017), who may display early white matter changes and functional
372 disability (Gupta et al., 2015). The human iPSC-based model described here exacerbates the defective
373 neuronal/glial development from NPCs reported in GLD murine models, and recapitulates the clinical
374 observations made on GLD patients. Also, several findings in this study suggest a composite and
375 mutation-dependent effect associated to GALC deficiency which impacts on NPC
376 commitment/differentiation besides psychosine toxicity: i) psychosine accumulation starts at early time
377 points of NPC differentiation and increases as cells differentiate into neurons and glia; still, this
378 progressive load is not accompanied by a dramatic increase of apoptotic cells; ii) higher percentages of
379 marker-negative cells are constantly found in GLD differentiated cultures, together with altered
380 expression of key genes involved in oligodendroglial, neuronal, and astroglial specification/maintenance,
381 suggesting a block in cell commitment or differentiation; iii) we observe only a partial rescue of the
382 differentiation program in LV.hGALC-transduced GLD neurons/glia - in which psychosine storage is
383 cleared - with an evident amelioration in the neuronal compartment but far less improvement in the
384 glial population.

385 In the attempt of elucidating the link between GALC deficiency and defective neural
386 differentiation, the mechanisms of disease correction upon gene transfer, and the mechanisms
387 underlying the mutation-specific phenotype, we pointed our attention on the lipidome. The
388 complexity and the many functions of the lipidome match, if not exceed, those of the genome or
389 proteome (Hannun and Obeid, 2017). Intriguingly, many sphingolipids involved in the GALC pathway,
390 such as ceramide, sphingosine, and sphingosine-1-phosphate, contribute to proliferation, migration, cell
391 fate, apoptosis (Hannun and Obeid, 2008, 2017) and, as suggested recently, senescence and autophagy
392 (Trayssac et al., 2018; Young and Wang, 2018). We previously documented the unbalance of some
393 bioactive lipids in brain tissues of GLD mice (Santambrogio et al., 2012). Here, we show a distinctive
394 global lipid profile in iPSCs vs. NPCs. vs. NPC progeny, regardless of the genotype (ND, GLD) or
395 mutation (GLD1, GLD5), suggesting a robust change in lipid metabolism during iPSC to neural
396 differentiation in our experimental conditions. In particular, the increase of SM levels during
397 differentiation in parallel with a decrease of PC might be related to the use of ceramide and PC by SM
398 synthases to produce SM (Liu et al., 2009).

399 By comparing the global lipidomic profile in each cell population, we observed that GLD and
400 ND cells differ for the abundance of various fatty acids and phospolipid classes. The mild unbalance of
401 lipid composition in GLD NPCs becomes more evident as cells differentiate. Intriguingly, GLD1 and GLD5

402 cell populations displayed remarkable differences in their lipidomic profile. Specifically, GLD5 iPSCs
403 and NPC progeny show an accumulation of TAG, DAG, and ceramide, whose role in cell fate, cellular
404 stress, ageing and replicative senescence has been proposed in multiple tissues and cell types (Hannun
405 and Obeid, 2002, 2017; Lizardo et al., 2017, 2018; Venable et al., 1995). We envisage that this peculiar
406 lipid perturbation contributes to the early senescence response and differentiation defects observed in
407 GLD5 iPSC-derived neural cells. Ceramide accumulation in GLD5 lines is counterintuitive, since
408 ceramide is the product of GalCer degradation by GALC. We speculate that other major pathways
409 leading to ceramide production may be induced in GLD5 cells, i.e. activation of sphingomyelinases
410 and/or ceramide synthases (Claus et al., 2009; Mullen et al., 2012). The SM-ceramide pathway is
411 particularly intriguing, since it may induce apoptosis, differentiation, and growth arrest (Jana et al., 2009).
412 SM might be converted into ceramide via sphingomyelinase to compensate GALC deficiency. Moreover
413 the parallel accumulation of DAG and TAG might be explained by an inhibition of the Kennedy pathway
414 that is essential for *de novo* glycerophospholipid biosynthesis and the SM cycle in sphingolipid
415 metabolism (Bieberich, 2012). Our data suggest that normalization of GALC activity rescues or at least
416 ameliorates the global lipid composition of mutant cells.

417 The association between lysosomal dysfunction, lipid unbalance, and senescence in NPCs,
418 neurons, and glial cells and its contribution to neurodegeneration and demyelination is emerging as an
419 area of active scientific investigations. Specifically, by taking advantage of mouse models or post-mortem
420 human brain samples it was reported that senescence functionally contributes to multiple sclerosis
421 pathogenesis (Nicaise et al., 2019) as well as to cognitive defects in Alzheimer disease (Zhang et al.,
422 2019). Notably, our study highlights the importance of performing this investigation in relevant human
423 iPSC-based neural models, which recapitulate the patient-specific pathological hallmarks more faithfully
424 as compared to murine models or non-neural cells.

425 Our study raises a number of relevant mechanistic questions. First, the respective role and
426 potential interaction between psychosine load and lipidome perturbation in determining the
427 different phenotype in GLD5 vs. GLD1 are not fully elucidated. One option would be the detrimental
428 action exerted by psychosine and ceramide (and possibly other lipid classes, e.g. TAG) preferentially
429 on oligodendrocyte and neuronal cells, respectively (Jana et al., 2009). Second, while our results
430 suggest an association between ceramide/TAG/DAG accumulation and senescence, the mechanistic
431 link between the GLD5 mutation and the occurrence of this specific lipid unbalance is not clear yet.
432 Possibilities include: i) a direct effect of the mutated GALC protein on the lipidome (the investigation
433 of the lipid-protein interactions and definition of the molecular mechanisms of pathway and enzyme

434 regulation are rapidly expanding in the field of bioactive lipids) (Hannun and Obeid, 2017); ii) an
435 indirect effect of another GLD-associated pathology (i.e. oxidative stress, mitochondrial dysfunction)
436 (Ricca and Gritti, 2016)(Ballabio and Gieselmann, 2009). It remains to be established which cell type is
437 mainly affected by these pathological hallmarks. Indeed, cellular stress and senescence programs
438 affect differently neurons, astrocytes and oligodendrocytes (Crowe et al., 2016).

439 In summary, our data show that GALC deficiency severely affects the differentiation of hiPSC-
440 derived neural progenitors into neurons, oligodendrocytes, and astrocytes. We highlight cell type-, and
441 patient-specific disease hallmarks in GLD cells, including galactosylsphingolipid storage, lipidome
442 perturbation, and activation of a senescence program. Finally, we show that a timely regulated GALC
443 expression is critical for proper neural commitment and differentiation. We anticipate these findings to
444 be starting point for future functional experiments aimed at further dissecting the complex and
445 mutation-specific GLD pathology. This knowledge will pave the way to tailored gene/cell therapy
446 strategies to enhance the correction of CNS pathology in GLD.
447

448 **Acknowledgments**

449 We are grateful to Lucia Sergi Sergi for LV preparation and titration, Andrea Ditadi for providing the ESC
450 line H9, Wim Kulik for psychosine analyses, Elizabeth Deane for providing the anti-hGALC antibody, all
451 the members of the Gritti's lab for generous support and helpful discussion.
452 Part of this work was carried out in ALEMBIC, an advanced microscopy laboratory established by IRCCS
453 Ospedale San Raffaele and Università Vita-Salute San Raffaele.
454 We thank the "Diagnosi PrePostnatale Malattie Metaboliche" Laboratory (G.Gaslini Institute) for
455 providing us with specimens from the "Cell line and DNA bank from patients affected by Genetic
456 diseases" Biobank - Telethon Genetic Biobank Network (project no. GTB07001A).
457

458 This study was funded by grants from Fondazione Telethon (Tiget Core Grant 2016-2021, grant D2) and
459 European Leukodystrophy Association (grant ELA 2016-010I3) to A.G.
460 R.D.M was supported by Fondazione Telethon (Tiget Core Grant 2016-2021, grant E5), a Career
461 Development Award from Human Frontier Science Program (HFSP), an Advanced Research Grant from
462 the European Hematology Association (EHA), "Pilot and Seed Grant 2015" from the San Raffaele
463 Hospital, a Hollis Brownstein Research Grant from Leukemia Research Foundation (LRF), the Interstellar
464 Initiative on Healthy Longevity from NYAS and AMED and by AIRC (MFAG 2019 - ID. 23321 project).
465 D.G was supported by the IBSA Foundation postdoctoral fellowship.

466 E.M., A.C., and L.d.V. conducted this study as partial fulfillment of their international Ph.D. in Molecular
467 Medicine, Vita-Salute San Raffaele University.
468

469 **Author contribution**

470 Conceptualization, A.G. and E.M.
471 Methodology, E.M, A.B, R.dM, S.M
472 Investigation, E.M., A.C, F.M., D.G., L.d.V., V.M., F.S., M.P, L.S.
473 Writing –Review & Editing, A.G., E.M, R.dM., A.B
474 Funding Acquisition, A.G.
475 Resources, S.M., A.B., R.dM., F.S.
476 Supervision, A.G., R.dM., A.B.
477

478 **Declaration of interests**

479 The authors declare no competing interests.
480

481 **Figure titles and legends**

482

483 **Figure 1. GLD iPSCs have undetectable GALC activity and increased psychosine levels (see also Figures**
484 **S1 and S2)**

485 A) Representative confocal immunofluorescence pictures of ND and GLD iPSCs expressing OCT4 (green),
486 NANOG (red), and TRA 1-60 (green). Nuclei are counterstained with Hoechst (blue). Single channels
487 (OCT4, NANOG, nuclei) and the merged picture (TRA 1-60/nuclei) are shown. Scale bars: 100μm.

488 B) Representative immunofluorescence pictures showing cells expressing endodermal (AFP),
489 mesodermal (α-SMA), and ectodermal (TUJ1) markers in ND and GLD embryoid bodies (EB). Lineage
490 markers in green, nuclei counterstained with Hoechst (blue). Scale bars: 80 μm (AFP) and 200 μm (TUJ1
491 and α-SMA).

492 C) GALC enzymatic activity in ND and GLD iPSC clones. Data are expressed as the mean ± SEM and
493 analyzed using Mann-Whitney test; ***p<0.001.

494 D) Psychosine levels measured by mass spectrometry in ND1 (white circles), ND2 (grey circles), and GLD
495 (colored circles) fibroblast cell lines (n=1 sample/line) and the corresponding iPSC clones (n=2 clones/line
496 in single or duplicate). Data are expressed as the mean ± SEM and analyzed by Mann-Whitney test
497 (Fibroblasts) and Kruskal Wallis test followed by Dunns' multiple comparison test (iPSCs); ns, not
498 significant * p<0.05, ***p<0.001 vs ND (all clones). The mean ± SEM of all ND and GLD clones are plotted
499 in the box and whiskers graph and analyzed by Mann-Whitney test; *p<0.05, ***p<0.001.

500

501 **Figure 2. LV-mediated gene transfer rescues GALC expression and enzymatic activity in GLD iPSCs (see**
502 **also Figure S3)**

503 A) Schematic representation of the LV.hGALC vector. hPGK, human phosphoglycerate kinase promoter;
504 wpre, Woodchuck hepatitis virus Post-transcriptional Regulatory Element.

505 B) Vector Copy Number measured in ND and GLD iPSCs clones transduced with LV.hGALC at multiplicity
506 of infection= 2 (MOI2). Data are expressed as the mean ± SEM (n=2-4 replicates/clone) and analyzed
507 using Kruskal Wallis test followed by Dunnett's multiple comparison post-test; *p<0.05.

508 C) GALC mRNA expression in untreated (UT; empty bars) and LV.hGALC-transduced (striped bars). n=3
509 replicates/clone. Values are normalized on GAPDH and expressed as fold change (2^-ΔΔCT) vs ND
510 (mean). Data are expressed as mean ± SEM and analysed using one way Anova followed by Turkey
511 multiple comparison post-test; **** p<0.0001.

512 D) Representative Western Blot showing the expression of the GALC-myc fusion protein (anti-myc
513 antibody; expected band size 80 kDa, indicative of the precursor protein) in LV.hGALC transduced (LV;
514 MOI2) ND and GLD iPSCs clones. β-actin was used as loading control. The 80kDa band is not detectable in
515 untransduced clones.
516 E) Representative immunofluorescence pictures showing the expression of the GALC protein (green;
517 anti-hGALC, recognizing the full-length protein) in untransduced (UT) and LV.hGALC transduced ND and
518 GLD iPSCs. Nuclei are counterstained with Hoechst (blue). Scale bars= 20μm.
519 F-G) GALC enzymatic activity (F) and Psychosine levels (G; clones as in F) in untransduced (UT, empty
520 bars) and LV.hGALC transduced (striped bars) ND, GLD and iPSCs. Data are expressed as the mean ± SEM
521 (n=2-4 replicates/clone). Data were analyzed by Kruskal Wallis test followed by Dunnett's multiple
522 comparison post-test (ND selected as control group); **p < 0.01; ***p < 0.001; ns, not significant.
523
524 **Figure 3. Differentiation of ND and GLD iPSCs into NPCs, neurons and glial cells**
525 A) Schematic representation of the protocol used to differentiate iPSCs into NPCs.
526 B) Downregulation of the expression of pluripotency-associated markers (NANOG, OCT4) and
527 upregulation of the expression of NPC markers (PAX6, DCX, ASCL1) in untransduced (UT) and LV.hGALC-
528 transduced ND and GLD iPSC-derived NPC populations (assessed by SYBR green RT-PCR). Data are
529 normalized on GAPDH expression and shown as fold change (2^-ΔΔCT) on the corresponding iPSC clone.
530 Data are expressed as the mean ± SEM (n=3-4 independent experiments; 2-3 replicates/clone). The
531 GLD1.3 clone (box) showed reduced upregulation of PAX6. Data analyzed using Kruskal Wallis test
532 followed by Dunnett's multiple comparison post-test (ND selected as control group). *p<0.05.
533 C) Representative immunofluorescence pictures showing the expression of the neural markers Nestin,
534 FOXG1 and PAX6 (green) in ND and GLD iPSC-NPC cultures. Nuclei are counterstained with DAPI (blue).
535 Scale bars=50μm.
536 D) Proliferation and stable expansion rate of untransduced and LV.hGALC transduced ND and GLD iPSC-
537 NPC lines (subculturing passages 0 to 5 shown in the graph; 16 days in vitro, DIV). Each point of the
538 curves is the mean ± SEM; n=2–3 independent experiments, 1-2 clones/group). Clones used: ND1.2,
539 ND1.3, ND2.1, ND2.2, GLD1.1, GLD1.3, GLD5.2, GLD5.6.
540 E) Schematic representation of the differentiation protocol used to differentiate iPSC-NPCs (d0) into
541 mixed neuronal/glial cultures that were analyzed in different experiments at day 7 (d7), d14, and d24.
542 GDM, Glial Differentiation Medium; GMM, Glial Maturation Medium.

F) GALC mRNA expression and G) GALC activity in untransduced (UT) and LV.hGALC-transduced iPSCs and neural progeny (NPCs, d0; differentiated cells, d14 and d24). Values in F) are normalized on GAPDH and expressed as (2^-ΔCT). Clones used: ND1.2, ND1.3, ND2.1, ND2.2, GLD1.1, GLD1.3, GLD5.2, GLD5.6

Data are expressed as the mean ± SEM (n=2-3 independent experiments; 1-2 replicates/clone). Data analyzed using two-way ANOVA. To compare the different time points (iPSC, NPC d0, differentiated cells, d14 and d24) in each group we used Turkey's multiple comparison post-test (*p < 0.05, **p < 0.01, ****p < 0.0001); to compare the different groups at each time point we used Dunnett's multiple comparison post-test (ND selected as control group). §p < 0.05, §§p < 0.01, §§§§p < 0.0001.

G) GALC enzymatic activity in untransduced (UT) and LV.hGALC-transduced ND and GLD iPSCs and neural progeny (NPCs, d0; differentiated cells, d14 and d24). Data are expressed as the mean ± SEM (n=2-4 replicates/clone). Data were analyzed by Kruskal Wallis test followed by Dunnett's multiple comparison post-test (ND selected as control group); *p < 0.01; ****p < 0.0001; ns, not significant.

H) Vector copy number (VCN) measured in LV.hGALC-transduced iPSCs and neural progeny (NPCs, d0; differentiated cells, d14). Clones used: ND2.2^{GALC}, GLD1.1^{GALC}, GLD5.2^{GALC}, GLD5.6^{GALC}; n= 1-3 independent experiments, 1-2 clones/group.

Figure 4. GLD NPCs display impaired neuronal and glial differentiation (see also Figures S4, S5, S6, S7)

A) Representative pictures of untransduced (UT) and LV.hGALC-transduced ND and GLD differentiated neural progeny (d24 of differentiation) expressing Olig2 (red) and APC (green). Nuclei are counterstained with Hoechst (blue). Scale bar, 50 µm.

B) Quantification of cells expressing Olig2 and APC in UT and LV.hGALC-transduced ND and GLD differentiated neural progeny (d14 and d24 of differentiation).

C) Representative pictures of UT and LV.hGALC-transduced ND and GLD differentiated neural progeny (d24 of differentiation) expressing TUJ1 (green; neurons) and GFAP (red; astrocytes). Nuclei are counterstained with Hoechst (blue). Scale bar, 50 µm.

D) Quantification of cells expressing TUJ1 and GFAP in UT and LV.hGALC-transduced ND and GLD differentiated neural progeny (d14 and d24 of differentiation).

Data in B and D are expressed as percentage of immunoreactive (IR) cells on total nuclei and represent the mean+SEM; n= 2-4 independent experiments; 1-3 clones/group with 2–3 replicates/clone for each time point; 5-10 fields/coverslips were analyzed. Clones used: ND1.2, ND2.1, ND2.2, GLD1.1, GLD1.3), GLD5.2, GLD5.6, ND2.2^{GALC}), GLD1.1^{GALC}, GLD5.2^{GALC}, GLD5.6^{GALC}). Data were analyzed by two-way ANOVA followed by Dunnett's multiple comparison post-test (ND at the corresponding time point selected as

575 control group). *p<0.05, **p<0.01, *** p < 0.001.

576

577 **Figure 5. Pathological hallmarks in GLD neural progeny**

578 A) Psychosine levels in UT and LV.hGALC-transduced ND and GLD NPCs (d0) and differentiated progeny
579 (d14 and d24). Data are expressed as mean+SEM, n=2-4 replicates/clone, 1-3 clones/group. Clones used:
580 ND1.2, ND2.1, ND2.2, GLD1.1, GLD1.3, GLD5.2, GLD5.6, ND2.2^{GALC}, GLD1.1^{GALC}, GLD5.2^{GALC}, GLD5.6^{GALC}.
581 Data were analyzed by two-way ANOVA followed by Turkey's multiple comparison post-test;
582 ****p<0.0001 GLD vs ND at the corresponding time point; #### p<0.0001 GLD vs GLD^{GALC} at the
583 corresponding time point. p>0.05 GLD^{GALC} vs ND at all time points.

584 B) Quantification of cells expressing cleaved caspase 3 (CC3) in UT and LV.hGALC-transduced ND and GLD
585 NPCs (d0) and differentiated progeny (d14 and d24 of differentiation). Data are expressed as percentage
586 of immunoreactive (IR) cells on total nuclei and represent the mean+SEM; n= 2 independent
587 experiments; 1-3 clones/group, 2–3 replicates/clone for each time point; 5-10 fields/coverslips were
588 analyzed. Clones used: ND1.2, ND2.1, ND2.2, GLD1.1, GLD1.3, GLD5.2, GLD5.6, ND2.2^{GALC}, GLD1.1^{GALC},
589 GLD5.2^{GALC}, GLD5.6^{GALC}. Data were analyzed by two-way ANOVA followed by Dunnett's multiple
590 comparison post-test (ND at the corresponding time point selected as control group). No differences
591 between groups (p>0.05).

592 C) PLA2 activity in untransduced and LV.hGALC-transduced ND and GLD NPCs (d0) and differentiated
593 progeny (d24 of differentiation). Data are expressed as mean+SEM. n=2 independent experiments; 1-3
594 clones/group. Clones used: ND1.2, ND2.1, ND2.2, GLD1.1, GLD1.3, GLD5.2, GLD5.6, ND2.2^{GALC},
595 GLD1.1^{GALC}, GLD5.2^{GALC}, GLD5.6^{GALC}.

596 D) Representative pictures of lysotracker-positive NPCs (red) and quantification of lysotracker-positive
597 area (μm^2/cell) in ND1.2, GLD1.3 and GLD5.6 clones. Nuclei are counterstained with Hoechst. Scale
598 bars= 20μm. Data are expressed as the mean+SEM, n=2 independent experiments, 3 wells/clone, 1.400-
599 12.000 cells/well were analyzed. Data analysed by two-way ANOVA followed by Dunnett's multiple
600 comparison post-test (ND selected as control group). *p<0,05.

601 E) Representative Western Blot and densitometric quantification showing the expression of the LAMP1
602 protein in UT and LV.hGALC-transduced ND and GLD NPCs (d0) and differentiated progeny (d7, d14 and
603 d24 of differentiation). β-actin was used as loading control. Data are represented as the mean+SEM; n=
604 2-3 independent experiments; 1-4 clones/group. Data were analyzed by two-way ANOVA followed by
605 Dunnett's multiple comparison post-test (ND at the corresponding time point selected as control group).
606 * p<0.05, **p< 0.01; **** p < 0.0001.

607

608 **Figure 6. GLD5 NPCs progeny display markers of senescence (see also Figure S8)**

609 A) Representative confocal immunofluorescence pictures and quantification of cells expressing nestin
610 (green) and Ki67 (red) in ND, GLD, and GLD^{GALC} NPCs (d0; shown in the pictures) and differentiated
611 cultures (d7 and d14 of differentiation). Nuclei are counterstained with Hoechst. Scale bars= 50μm. Data
612 in the graph are expressed as the mean+SEM n= 3 independent experiments; 1-3 clones/group with 1–3
613 replicates/clone for each time point; 5-10 fields/coverslips were analyzed. Clones used: ND1.2, ND1.3,
614 ND2.1, ND2.2, GLD1.1, GLD1.3, GLD5.2, GLD5.6).

615 B) Quantification of EdU positive cells (after a 16 hour-pulse) in ND, GLD, and GLD^{GALC} NPCs (d0) and
616 differentiated cultures (d7 and d14 of differentiation). Data in the graph are expressed as percentage
617 over total cells (mean); n= 2 independent experiments for each time point, 1-2 clones/group. Clones
618 used: ND1.2, ND2.2, GLD1.1, GLD5.2, GLD5.6, GLD1.1^{GALC}, GLD5.2^{GALC}.

619 C) Expression of p21 mRNA in ND, GLD, and GLD^{GALC} NPCs (d0) and differentiated cultures (d14 of
620 differentiation). n= 4 independent experiments; 1-2 clones/group. Clones used: ND1.2, ND2.2, GLD1.1,
621 GLD1.3, GLD5.2, GLD5.6, GLD1.1^{GALC}, GLD5.2^{GALC}, GLD5.6^{GALC}. Data are normalized on the housekeeping
622 gene glucuronidase β (*GUSB*) and expressed as $2^{-\Delta CT}$. Data are represented as mean+SEM. Data were
623 analyzed by Kruskal Wallis test followed by Dunns' multiple comparison post-test (ND at the
624 corresponding time point selected as control group). * $p<0.05$.

625 D) Representative Western blot and densitometric quantification showing the expression of the p21
626 protein in ND, GLD, and GLD^{GALC} NPC differentiated progeny at d7 and d14 of differentiation (d14 shown
627 in the blot). Calnexin was used as loading control. Data are expressed as fold vs ND at the corresponding
628 time point (mean of all clones) and represented as the mean+SEM; n= 2 independent experiments; 1-3
629 clones/group. Clones used: ND1.2, ND2.2, GLD1.1, GLD1.3, GLD5.2, GLD5.6, GLD1.1^{GALC}, GLD5.2^{GALC},
630 GLD5.6^{GALC}. Data were analyzed by two-way ANOVA followed by Dunnett's multiple comparison post-test
631 (ND at the corresponding time point selected as control group). * $p<0.05$.

632 **E)** Representative confocal immunofluorescence pictures and quantification for 53BP1-positive DDR foci
633 in ND, GLD, and GLD^{GALC} NPC (d0) and differentiated cultures (d7 and d14 of differentiation; d14 shown
634 in the pictures). Nuclei are counterstained with DAPI. Scale Bar = 15 µm (for all panels, shown in ND).
635 Clones used: ND1.2, ND2.2, GLD1.1, GLD1.3, GLD5.2, GLD5.6, GLD1.1^{GALC}, GLD5.2^{GALC}, GLD5.6^{GALC}. Data in
636 the graph are expressed as the mean+SEM; n= 3 independent experiments, 2-3 replicates/clone for each
637 time point. 100 to 600 nuclei per condition were analyzed. Data were analyzed by Kruskal Wallis test

638 followed by Dunns' multiple comparison post-test (ND at the corresponding time point selected as
639 control group). * $p<0.05$, ** $p < 0.01$.
640 **F)** Representative pictures (brightfield and immunofluorescence for nuclei) and quantification of SA-
641 βGal-positive cells in ND, GLD, and GLD^{GALC} NPCs (d0) and differentiated cultures (d7 and d14 of
642 differentiation; d7 shown in the pictures). Nuclei are counterstained with Hoechst. Scale bars= 50μm (for
643 all panels, shown in ND). Data in the graph are expressed as the mean+SEM n= 3 independent
644 experiments; 1-3 clones/group, 1–3 replicates/clone for each time point; 4-10 fields/coverslips were
645 analyzed. Clones used: ND1.2, ND2.1, ND2.2, GLD1.1, GLD5.2, GLD5.6, $GLD1.1^{GALC}$, $GLD5.2^{GALC}$,
646 $GLD5.6^{GALC}$. Data were analyzed by two-way ANOVA followed by Dunnett's multiple comparison post-test
647 (ND at the corresponding time point selected as control group). * $p<0.05$.
648
649 **Figure 7. Lipidomic profile during iPSC neural differentiation (see also Figure S9)**
650 A) Hierarchical clustering of lipid species differently enriched in iPSCs, NPCs and differentiated cultures
651 (d14). ANOVA statistical test was applied (FDR<0.05).
652 B) Hierarchical clustering of lipid species differently enriched in ND, GLD1 and GLD5 iPSCs, NPCs and
653 differentiated cultures (d14 of differentiation). ANOVA statistical test was applied (FDR<0.05).
654 C) Principal component analysis (PCA) of lipid species distribution in ND, GLD and LV.hGALC transduced
655 GLD iPSCs, NPCs and differentiated cultures (d14 of differentiation). Clones used: ND2.2, GLD1.1, GLD5.2,
656 $ND2.2^{GALC}$, $GLD1.1^{GALC}$, $GLD5.2^{GALC}$. See methods for abbreviation of lipid classes.
657

658 **Methods**

659 Reagents generated in this study are available upon request from the Lead Contact with a completed
660 Materials Transfer Agreement.

661 The lipidomic dataset generated during this study is uploaded at MetaboLights, weblink
662 https://www.ebi.ac.uk/metabolights/MTBLS1501. The public release date is set to Feb 15 00:00:00 GMT
663 2021.

664

665 **Generation of iPSCs from human fibroblasts**.

666 Human dermal fibroblasts from healthy donors (ND1 and ND2) were purchased from Life technologies.
667 Fibroblasts from GLD patients (GLD1, GLD2, GLD3, GLD4, and GLD5) and of a non-affected relative of
668 GLD1 (ND3) were obtained from the Cell Line and DNA Bank of Patients affected by Genetic Diseases
669 (Gaslini Institute, Genova, Italy). Human fibroblasts were cultured in Dulbecco's modified Eagle's
670 medium (DMEM) supplemented with 10% fetal bovine serum (FBS), L-glutamine, and
671 penicillin/streptomycin in an humidified atmosphere, 5% CO_2 at 37°C. Fibroblasts at passages (p) 4-5
672 (GLD1, GLD2, GLD3, ND1, ND2) and p10-11 (GLD4 and GLD5, ND3) were used for reprogramming.

673 Reprogramming was outsourced to BioERA (Padova, Italy). Reprogramming factors were delivered as
674 modified mRNAs (mmRNAs) taking advantage of a microfluidic system (Luni et al., 2016). The StemMACS
675 mRNA Reprogramming Kit (Miltenyi Biotec, Bergisch Gladbach, Germany) was used for mRNA
676 transfection according to the manufacturer instructions. Colonies positive for NANOG and TRA-1-60
677 were catalogued as iPSCs with progressive numbering. Six randomly selected colonies/donor were
678 picked and expanded for 2 passages. Cells were then frozen; two frozen vials/donor were sent to SR-
679 Tiget. The iPSCs obtained from BioERA were thawed and cultured on matrigel-coated (BD Biosciences,
680 Erembodegen, Belgium) plastic dishes in StemMACS™ iPS-Brew XF medium (Miltenyi Biotech) in an
681 humidified atmosphere, 5% O_2, 5% CO_2 at 37°C. The medium was changed daily. For routine passage,
682 cells were detached in PBS containing 0,5 mM EDTA and split at 1:3 to 1:10 ratio. Accutase (Sigma-
683 Aldrich, Saint Louis, USA) was used for single cell dissociation of iPSC colonies.

684 Human cells were used according to the guidelines on human research issued by the San Raffaele
685 Scientific Institute's ethics committee (protocol TIGET-HPCT).

686

687 **Karyotype analysis.**

688 Karyotyping was performed as previously described (Meneghini et al., 2017). Briefly, iPSC cultures were
689 treated with KaryoMAX colcemid 0,1 mg/ml (Life Technologies, Carlsbad, USA) for 2 h at 37°C. After

690 hypotonic treatment with 0,075 M KCl and fixation in methanol: acetic acid (3:1), the cell suspension was
691 dropped onto a microscopy slide and air-dried. Chromosome counts and G-banding karyotype analyses
692 were done on metaphases stained with Vectashield mounting medium with DAPI (Vector Laboratories,
693 Burlingame, USA). Images were analysed with Applied Imaging Software CytoVision (CytoVision Master
694 System). We counted >10 metaphases/coverslip. The karyotype is considered normal when >90% of the
695 counted metaphases are normal (46, XX or 46, XY).
696
697 **Embryoid Bodies formation.**
698 iPSC colonies were gently detached using a scraper, dissociated in small cell clumps using a 2ml pipette,
699 plated in Ultra-low attachment plates (Corning, New York, USA) and grown in suspension for 10 days in
700 EB medium: DMEM-F12+20% Knockout Serum Replacement (KSR), non-essential aminoacids, Sodium
701 Piruvate, L-glutamine, penicillin/streptomycin and 0,1 mM β-mercaptoethanol. The resulting spheroids
702 were allowed to reattach on matrigel-coated 6-well plates or glass coverslips to continue differentiation
703 for additional 10 days. Finally, they were collected for RNA extraction or fixed with 4% paraformaldehyde
704 (PFA) for immunofluorescence analyses.
705
706 **iPSCs differentiation into NPCs**.
707 For neural induction of iPSCs we applied a dual-smad inhibition protocol (Chambers et al., 2009, 2011).
708 Briefly, iPSC colonies were detached using Accutase, suspended as single cells and plated on Matrigel-
709 coated dishes (75,000 cells/cm^2) in StemMACS™ iPS-Brew XF medium supplemented with 10 µM of
710 ROCK inhibitor Y-27632 (Sigma-Aldrich). At ≈90% confluence (usually 2 days after plating), culture
711 medium was replaced with KSR medium (Chambers et al., 2009, 2011) supplemented with 200 ng/ml of
712 recombinant human Noggin (R&D Systems, Minneapolis, USA) and 10 µM of SB431542 (Sigma-Aldrich).
713 The medium was changed daily for the next 3 days. At day 4, KSR medium was gradually switched to N2
714 medium (Chambers et al., 2009, 2011) containing Noggin and SB431542 (75-25%, 50-50%, 25-75% every
715 two days). After 10 days, cells were detached using Accutase and plated on Matrigel-coated dishes in N2
716 medium supplemented with 20 ng/ml bFGF, 20 ng/ml EGF and 10 µM Y-27632. In these conditions, the
717 newly generated NPCs can be expanded for 4-6 passages. For all the differentiation experiments we used
718 NPCs at passages 2-3.
719
720 **Assessment of long-term cell proliferation.**

721 iPSCs or NPCs were dissociated with Accutase and plated at a density of 30,000 or 50,000 cells/cm^2,
722 respectively, in the appropriate medium supplemented with 10 µM Y-27632. After 4 days, or in any case
723 at full cell confluence, cells were treated with Accutase and counted. Cells were then replated at the
724 initial density. The procedure was repeated for at least 4 passages.
725
726 **iPSC-NPCs differentiation into mixed neuronal/glial cultures**.
727 We applied a published protocol (Frati et al., 2018) with some modifications. Cells were detached using
728 Accutase and plated on Matrigel-coated dishes (20,000 cells/cm^2) in N2 medium with 20 ng/ml bFGF, 20
729 ng/ml EGF and 10 µM Y-27632 (d0). Two days after plating and for the subsequent 4 days we gradually
730 replaced N2 medium with increasing amount of Glial Differentiation Medium (GDM) containing 10 ng/ml
731 PDGF-AA, 10 ng/ml NT3, 10 ng/ml IGF-1, 5 ng/ml HGF, and 60 ng/ml T3. From d4 to the end of the
732 differentiation protocol (d24) medium was changed every other day. From d14 to day 24 cells were kept
733 in Glial Maturation Medium (GMM) in absence of growth factors and supplemented with 20 µg/ml of
734 ascorbic acid (Sigma-Aldrich).
735
736 **Lentiviral vector-mediated *hGALC* gene transfer in iPSCs.**
737 We used a previously described (Meneghini et al., 2016) third-generation lentiviral vector (LV) encoding
738 the human (h)GALC cDNA tagged with the myc peptide, under control of the human phosphoglycerate
739 kinase (PGK) promoter. The titer of the LV batch was 1.6x10^9 TU/ml. For cell transduction, iPSC colonies
740 were dissociated at single cells using Accutase and plated on Matrigel-coated 6 multiwell plates (10,000
741 cells/cm^2) in StemMACS™ iPS-Brew XF medium supplemented with 10 µM Y-27632. After 6 hours, cells
742 were incubated with LV.hGALC vector at different MOI (0-100) in StemMACS™ iPS-Brew XF medium
743 additioned with 10 µM Y-27632 and 8 µg/ml Polybrene. After an obvernight incubation, we added fresh
744 culture medium. Cells were passaged as they reached confluency, as described. Transduced cells were
745 used for the experiments after 3-4 subculturing passages, in order to dilute the non-integrated LV
746 genome.
747
748 **Quantification of Psychosine**.
749 Psychosine quantification was performed on frozen cell pellets by TSQ Quantum AM mass spectrometer
750 (Thermo Fisher Scientific, Waltham, USA) as previously described (Lattanzi et al., 2014).
751
752 **GALC activity assay**

753 Specific beta-galactocerebrosidase activity was measured by hydrolysis of artificial fluorogenic substrate
754 4-methylumbelliferone-beta-galactopyranoside in presence of the competitive inhibitor of beta-
755 galactosidase $AgNO_3$, as previously described (Martino et al., 2009).
756
757 **PLA2 activity assay**
758 Quantification of Phospholipase A2 (PLA2) activity was performed using the EnzChek Phospholipase A2
759 Assay Kit (Thermo Fisher). 50 µl of cell lysate/well, corresponding to 20 µg total proteins, was mixed with
760 50 µl of substrate cocktail to initiate the catalytic reaction. After 10 minutes, fluorescence was measured
761 using a Victor3 Multilabel Counter (Perkin Elmer, Waltham, USA) at 360 nm (excitation) and 460 nm
762 (emission). The specific enzymatic activity was calculated for each sample and normalised for protein
763 content. Values are expressed as relative fluorescent units (RFU)/µg of protein/min.
764
765 **SA-β-Galactosidase assay (X-gal staining).**
766 Induction of senescence during NPCs differentiation was assessed with a senescence β-galactosidase (SA-
767 β-Gal) Staining Kit (Cell Signalling Technology, Danvers, USA) according to manufacturer's instructions. In
768 detail, NPCs were plated on coverslips and fixed at day 0, day 7 and day 14 days of differentiation
769 with4% PFA for 10 minutes at RT and then incubated for 24 hours with the SA-β-gal staining solution
770 (pH=6.0) to reveal SA-β-gal activity. Nuclei were then stained with Hoechst. Images were acquired using
771 a Nikon Eclipse Ni microscope, visualized and analysed using the ImageJ software. Cells displaying blue
772 signal in the cytosol were counted as positive. At least 850 nuclei/coverslip/timepoint were used for
773 quantification.
774
775 **Proliferation analysis (EdU staining)**
776 EdU (5-ethynyl-2'-deoxyuridine), supplied with Click-iT EdU Alexa Fluor 647 Imaging Kit (Thermo-Fisher
777 Scientific), was diluted in DMSO to a final concentration of 10 mM and kept at −20°C. Cells were
778 incubated with 2µM EdU overnight in culture. $2x10^5$ cells per sample were transferred to cytometry
779 tubes and then washed with PBS 1% BSA and fixed with 100 µL of Click-iT fixative for 15 minutes. Cells
780 were washed again with PBS 1% BSA and permeabilized with 100 µL of 1X Click-iT saponin-based solution
781 for 15 minutes. Detection of EdU-DNA was performed by incubating cells with 500 µL of Click-iT Plus
782 reaction cocktail for 30 minutes at RT protected from light. Cells were subsequently washed with PBS 1%
783 BSA and fluorescence was measured by flow cytometry.
784

785 **High Throughput live cell Microscopy**

786 Determination of lysosomal area was performed using a high content imaging platform in the Advanced
787 Light and Electron Microscopy Bio-Imaging Centre of San Raffaele Scientific Institute (ALEMBIC) using the
788 ArrayScan XTI HCA Reader from Thermo Fisher Scientific. Cells were plated on matrigel-coated 96
789 Greiner Sensoplate glass bottom multiwell plates (Sigma Aldrich) (30,000 cells/well). The day after
790 plating, cells are incubated with 50 nM LysoTracker Red DND-99 (Thermo Fisher) diluted in culture
791 medium, for 30 minutes at 37°C. Nuclear staining, necessary for the instrument acquisition and analysis,
792 was performed using Hoechst (5 min at room temperature, 10 µg/ml final concentration). Cells are then
793 washed with Krebs-Ringer-Hepes-bicarbonate buffer (KRH) and maintained in the same buffer for the
794 entire duration of the instrument acquisition. Thirty fields were acquired for each well; images were
795 analysed with the Thermo Scientific HCS Studio Cell Analysis Software

796

797 **Immunofluorescence.**

798 Cells are seeded in 48-multiwell plates on Matrigel-coated 10 mm round sterile glass coverslips, fixed in
799 4% PFA, rinsed with PBS, incubated with blocking solution containing 10% normal goat serum (NGS) +
800 0.1% Triton X-100 in PBS for 45 minutes and incubated overnight at 4°C with primary antibodies diluted
801 in blocking solution. After 3 washes (10 minutes each), cells are incubated with species-specific
802 fluorophore-conjugated secondary antibodies diluted in 1% NGS in PBS for 1 hour at room temperature.
803 Cell nuclei are counterstained with Hoechst (10µg/ml, diluted in PBS). Finally, coverslips are mounted on
804 glass slides using Fluorsave mounting medium (Merck Millipore). Samples incubated in blocking solution
805 without primary antibodies were used as negative controls. Images were obtained with a Nikon Eclipse
806 Ni microscope, visualized and analysed using the ImageJ software.

807 To evaluate DDR activation during NPCs differentiation, cells were fixed with 4% PFA for 20 min at RT
808 and then permeabilized with 0.3% Triton-X100 in PBS for 10 min. After washing, coverslips were blocked
809 in PBG (0.2% cold water fish gelatine, 0.5% BSA in PBS) for 30 min. Cells were then stained with primary
810 antibodies 1 hour at RT followed by secondary antibodies. After DAPI staining (Sigma-Aldrich), slides
811 were mounted with Aqua-Poly/mount (Polysciences Inc, Warrington, USA). Images were obtained with
812 Leica TCS SP5 confocal laser microscope and visualized with Leica Application Suite (LAS) software (Leica
813 Microsystems, Wetzlar, Germany). Quantification of DDR activation in immunofluorescence images was
814 conducted by counting colocalizing foci for 53BP1 and γH2A.X.

815 Primary and secondary antibodies used:

816

817

Primary antibodies		
Antigen	**Host species (company, catalog number)**	**Dilution**
53BP1	Rabbit polyclonal (Bethyl, A300-272A-5)	1: 600
α-fetoprotein	Mouse monoclonal (Abcam, AB3980)	1: 200
α-Smooth Muscle Actin	Mouse monoclonal (Sigma-Aldrich, C6198)	1: 400
APC	Mouse monoclonal (Calbiochem, OP80)	1: 300
β-III tubulin (TUJ1)	Mouse monoclonal (Biolegend, 801202)	1: 1,000
γH2A.X	Mouse monoclonal (Biolegend, 613402)	1: 200
Cleaved Caspase 3	Rabbit polyclonal (Cell Signaling, 9961)	1: 200
FOXG1	Rabbit polyclonal (Abcam, AB 18259)	1: 300
GALC	Mouse monoclonal, kindly provided by Dr. Deane	1: 20
GalCer	Mouse monoclonal (Millipore MAB342)	1: 300
GFAP	Rabbit polyclonal (DAKO, ZO334)	1: 1,000
Ki67	Rabbit polyclonal (Novocastra, NCL-Ki67-p)	1: 200
NANOG	Rabbit polyclonal (Abcam, AB21624)	1: 200
Nestin	Mouse monoclonal (Millipore, MAB353)	1: 500
OCT4	Rabbit monoclonal (Abcam, AB136253)	1: 300
Olig2	Rabbit monoclonal (Abcam, AB136253)	1: 300
PAX6	Rabbit polyclonal (Covance, PRB-278P)	1: 300
TRA 1-60	Mouse monoclonal (Millipore, MAB4360)	1: 100
Secondary antibodies		
Conjugate	**Host species (company, catalog number)**	**Dilution**
Alexa 488	Goat anti-mouse and Goat anti-rabbit IgG (Mol.Probes, A11001 and A11008)	1: 1,000
Alexa 546	Goat anti-mouse and Goat anti-rabbit IgG (Mol.Probes, A11003 and A11010)	1: 2,000
Alexa 568	Goat anti-rabbit IgG (Mol.Probes, A11031)	1: 2,000

818

819 **Western blot analysis.**

820 Cell pellets were lysed using RIPA buffer (50 mM Tris–HCl pH 7,4, 150 mM NaCl, 0,5% sodium
821 deoxycholate, 0,1% SDS, 2 mM EDTA) containing protease and phosphatase inhibitors (Roche, Basel,
822 Switzerland). Protein content was measured using the Bradford reagent (Bio-Rad, Hercules, USA) with
823 bovine serum albumin (BSA) as the reference standard. SDS-PAGE of protein extracts was performed
824 using Novex NuPAGE SDS-PAGE system (Thermo Fisher Scientific) according to manufacturer instructions.
825 Proteins were transferred on PVDF membranes (Millipore, Burlington USA) for 1 hour at 400mA.
826 Primary and secondary antibodies used:

827

Primary antibodies		
Antigen	**Host species (company, catalog number)**	**Dilution**
α-tubulin	Mouse monoclonal (Sigma-Aldrich, T6074)	1: 5,000
Acetylated α-tubulin	Mouse monoclonal (Sigma-Aldrich, T7451)	1: 20,000
β-Actin	Rabbit polyclonal (Santa Cruz, sc-1616r)	1: 10,000
β-Actin	Mouse monoclonal (Sigma-Aldrich, A2228)	1: 10,000
β-III tubulin (TUJ1)	Mouse monoclonal (Biolegend,801202)	1: 6,000
Calnexin	Rabbit polyclonal (Sigma-Aldrich, c4731)	1: 10,000
GFAP	Mouse monoclonal (Millipore, MAB3402)	1: 100,000
LAMP1	Rabbit polyclonal (Abcam, AB24170)	1: 6,000
MYC	Rabbit polyclonal (Abcam, AB9106)	1: 5,000
Neurofilament-M (RMO 14.9)	Mouse monoclonal (Cell Signaling, 2838)	1: 1,000
OLIG1	Rabbit polyclonal (Millipore, AB5591)	1: 800
p21	Rabbit monoclonal (Cell Signaling, 2947)	1: 1,000
Polyglutamylation Modification	Mouse monoclonal (Adipogen, AG-20B-0020)	1: 5,000
SMI 311	Mouse monoclonal (Sternberg, SMI-311)	1:1000
SMI 312	Mouse monoclonal (Covance, SMI312R)	1:1000
Secondary antibodies		
Conjugate	**Host species (company, catalog number)**	**Dilution**
HRP	Goat anti-mouse IgG (Chemicon, AP124P)	1: 5,000
HRP	Goat anti-rabbit IgG (Millipore, 12-348)	1: 10,000

828

829 **Molecular analysis**

830 ***Sequencing of patient's mutations.*** Genomic DNA was extracted from iPSCs pellets using Maxwell cell
831 DNA purification Kit (Promega), following the manufacturers' instructions. DNA concentration was
832 determined by 260/280nm optical density (OD) reading on a NanoDrop ND-1000 Spectrophotometer
833 (NanoDrop, Pero, Italy). To confirm the presence of the expected mutations in the *GALC* gene of GLD
834 patients-derived cells, the regions of interests were amplified by PCR, purified from agarose gels using
835 the Wizard SV Gel and PCR Clean-Up System (Promega, Madison, USA) and sent for sequencing (to GATC
836 Services-Eurofin Genomics, Ebersberg, Germany). Sequences were checked using the Snapgene
837 software. Three primer PCR to confirm 30kb deletion in GLD1 and GLD3 cells was performed as described
838 by (Liu et al., 2011). Primers used for PCR amplification and sequencing are the following:

839

840

Primers for gDNA sequencing	
GALC region	**Sequence**
INTRON 11	Fw 5' - CCTATATGGAAAACAATGTGG - 3',
	Rev 5' - AAGGAGCAACATTTCAGGC - 3' (WT allele)
	Rev 5' - TCAAGTCCTTGATGATCACC - 3' (deleted allele)
EXON 4	Fw 5'- GGTGGGGAGTGAGATGGTC - 3',
	Rev 5' - CAAGGGCAAAGAAAGGATCA - 3'
EXON 8	Fw 5' - TGCTGAGACAAAAGGGCATA - 3',
	Rev 5' - GATGACGCTAACAAGGCAAA - 3'
EXON 9	Fw 5' - TTGGGTGATCCTTTTATTGTCA -3',
	Rev 5' - CACTGGCAAATCTTGCTTAAAA - 3'
EXON 14	Fw 5' - AGCAAGGAGAGCTTCTGAAGGA - 3',
	Rev 5' - AGGTTCTTGAAATAGGAGGACCA - 3'

Gene expression analysis: RT-PCR; SYBR green and TaqMan RT-PCR. Total RNA was extracted using the RNeasy Mini Kit (Qiagen). RNA was quantified by 260/280nm optical density (OD) reading on a NanoDrop ND-1000 Spectrophotometer (NanoDrop, Pero, Italy). mRNA reverse transcription (RT) is performed with QuantiTect reverse transcription kit (Qiagen, Hilden, Germany).

RT-PCR analyses were performed by using FastStart Taq DNA Polymerase, PCR KIT (Roche). For each reaction, 100 ng of template cDNA and 1 mM of primers were used. PCR products were resolved by electrophoresis in a 1,5% agarose gel.

Quantitative real time PCR reactions were performed in Optical 96-well Fast Thermal Cycling Plates (Primo 96-well plates, Euro Clone, Pero, Italy) on Viia7 quantitative real time PCR system (Applied Biosystem, Foster City, USA), using the following thermal cycling conditions:

- SYBR green qPCR: one cycle at 95°C for 2 minutes, 40 cycles at 95°C for 10 seconds and 60°C for 30 seconds; each sample is run in duplicate in a total volume of 12.5 µl/reaction, containing 6.25 µl 2X Fast SYBR Green Master Mix (Qiagen), 10 ng of template cDNA, and10µM of custom primers were used. As internal reference for normalization GAPDH was used

- TaqMan qPCR: one cycle at 95°C for 5 minutes, 40 cycles at 95°C for 50 seconds and 60°C for 1 minute. Each sample is run in duplicate in a total volume of 12.5 µl/reaction, containing 6.25 µl 2X EagleTaq Universal Master Mix (Roche), 1µl of sample cDNA and 0.63µl of Probe+Primers mix (TaqMan Gene Expression Assays, Thermo Fisher). The Viia7 software was used to extract raw data. Relative expression of mRNA for the target genes was calculated using the comparative Ct (ΔΔCt) method, with a housekeeping gene as control. Raw data (Ct values) were analyzed according to the comparative Ct

862 method. For gene expression data, analyses were performed on $2(-^{\Delta Ct})$ values relative to housekeeping
863 gene or plotted as $2^{-\Delta\Delta Ct}$ (fold change), as specified in figure legends. Primers and probes used for gene
864 expression analyses are the following:

Primers for RT-PCR	
Gene	**Sequence**
KLF4	Fw 5 ’ -ACCCACACAGGTGAGAAACCTT - 3’
	Rev 5’ - GTTGGGAACTTGACCATGATTG - 3’
SOX2	Fw 5’ - TTACCTCTTCCTCCCACTCCAG - 3’
	Rev 5’ - GGGTTTTCTCCATGCTGTTTCT - 3’
NANOG	Fw 5’- GAT CGG GCC CGC CAC CAT GAG TGT GGA TCC AGC TTG-3’
	Rev 5’- GAT CGA GCT CCA TCT TCA CAC GTC TTC AGG TTG - 3’
CD146	Fw 5’- AAG GCA ACC TCA GCC ATG TC - 3’
	Rev 5’- AGA AGA TGC GCT CGT CTT GG - 3’
CXCR4	Fw 5' - CAG CAG GTA GCA AAG TGA CG - 3'
	Rev 5' - TTG TCC GTC ATG CTT CTC AG - 3'
MAP2	Fw 5' - AAG AAG GTC GCC ATC ATA CG - 3'
	Rev 5' - GGG CTT TAG CAT GCT CTC TG - 3
PAX6	Fw 5’ - AAC AGA CAC AGC CTT CAC AAA CA - 3’
	Rev 5’ - CGG GAA CTT GAA CTG GAA CTG AC - 3’
SOX17	Fw 5’ - TTC ATG GTG TGG GCT AAG GAC - 3’
	Rev 5’ - AGT TGG GGT GGT CCT GCA TG - 3’
α-SMA	Fw 5’ - GTG TTG CCC CTG AAG AGC AT - 3’
	Rev 5’ - GCT GGG ACA TTG AAA GTC TCA - 3’
GAPDH	Fw 5' - CAG CCT CAA GAT CAT CAG CA - 3'
	Rev 5' - TGC TGT AGC CAA ATT CGT TG - 3'
Primers for SYBR-green RT-PCR	
Gene	**Sequence**
ASCL1	Fw 5' - TCCCCCAACTACTCCAACGA - 3'
	Rev 5' - GCGATCACCCTGCTTCCAAA - 3'
CDKN1A	Fw 5' - CAGCATGACAGATTTCTACCACTC - 3'
	Rev 5' -CTCGCGCTTCCAGGACTG - 3'
CDKN2A	Fw 5' - CCAACGCACCGAATAGTTACG - 3'
	Rev 5' - GCGCTGCCCATCATCATG - 3'
DCX	Fw 5' - TGGATGAAAATGAATGCCGAGT - 3'
	Rev 5' - AGCTGGAGACTTGCTTCGG - 3'
GAPDH	Fw 5' - TCAAGAAGGTGGTGAAGCAGG - 3'
	Rev 5' - ACCAGGAAATGAGCTTGACAAA - 3'

GUSB	Fw 5' - CTGACACCTCCAAGTATCCCAAG - 3'
	Rev 5' - GTCGTGTACAGAAGTACAGACCGC - 3'
IL1β	Fw 5' - GCTCAAGTGTCTGAAGCAGCC - 3'
	Rev 5' - CAGCTTCAAAGAACAAGTCATCCT - 3'
NANOG	Fw 5' - ATGCCTCACACGGAGACTGT - 3'
	Rev 5' - AAGTGGGTTGTTTGCCTTTG - 3'
OCT4	Fw 5' - TCGAGAACCGAGTGAGAGG - 3'
	Rev 5' - GAACCACACTCGGACCACA - 3'
PAX6	Fw 5' - AGTGAATCAGCTCGGTGGTGTCTT - 3'
	Rev 5’ - TGCAGAATTCGGGAAATGTCGC - 3'
TNF-α	Fw 5' – CCAGGGACCTCTCTCTAATCAGC - 3'
	Rev 5’ – GGTTTGCTACAACATGGGCTAC - 3'
Probe+Primers for Taqman RT-PCR	
Gene	**Commercial Code**
DCX	Hs00167057_m1
GALC	Hs01012300_m1
GAPDH	Hs02758991_g1
GFAP	Hs00157674_m1
KLF4	Hs00358836_m1
MBP	Hs00921945_m1
NANOG	Hs02387400_g1
NEUROD1	Hs01922995_s1
NKX2.2	Hs0159616_m1
OLIG2	Hs00300164_s1
OCT4	Hs03005111_g1
PDGFRα	Hs00183486_m1
SCL1A3	Hs00904823_g1
SOX2	Hs01053049_s1
SOX10	Hs00366918_m1

Determination of vector copy number (VCN)

Genomic DNA was extracted from cell pelletes using Maxwell cell DNA purification Kit (Promega) or QIAamp DNA Micro Kit (Quiagen), depending on the number of cells. The number of integrated vector copies/genome was quantified by TaqMan analysis, as previously described (Lattanzi et al., 2010). Briefly, quantitative PCR was performed on 50 ng of template DNA using probes and primers that anneal to the PSI (ψ) sequence of the LV backbone and to a fragment of the human telomerase gene. A standard curve was set up with gDNA extracted from a human lymphoblast cell line (CEM) carrying 1

873 copy of integrated LV.GFP, validated by Southern blot analysis. The standard curve, based on different
874 dilutions of CEM gDNA (from 0,32 ng to 40 ng) was used for both LV and telomerase amplification.
875 Reactions were carried out in a total volume of 25 µl, on Viia7 quantitative real time PCR system (Applied
876 Biosystem). Eventually, VCN is calculated as: (ng LV/ng endogenous DNA) × (number of LV integrations in
877 the standard curve) × cell ploidy. Primers and probes used for VCN analyses are the following:

Primers for VCN assay		
Gene	**Probe sequence**	**Primer sequence**
HIV	5'- ATCTCTCTCCTTCTAGCCTC - 3'	For 5' – TACTGACGCTCTCGCACC - 3'
		Rev 5' – TCTCGACGCAGGACTCG - 3'
TELO	5' -TCAGGACGTCGAGTGGACACGGTG- 3'	For 5' – GGCACACGTGGCTTTTCG - 3'
		Rev 5' – GGTGAACCTCGTAAGTTTATGCAA - 3'

878

879 **Lipidomic analyses**

880 ***Lipid extraction***. Cell pellets were resuspended in 150 mM Ammonium bicarbonate and passed through
881 a 26G syringe needle to prepare cell lysate. Lipids were extracted starting from an equivalent of 10 µg of
882 proteins, using a 2 steps extraction protocol (Folch method) with methanol and chloroform in different
883 proportions (FOLCH et al., 1957). Organic phase fractions were then dried out and resuspended in 50 µL
884 of CH3OH for subsequent analysis. Before extraction, samples were spiked in with 16 internal standards:
885 PC (12:0/13:0) 40 pmol, PE (12:0/13:0) 52 pmol, PG (12:0/13:0) 7.5 pmol, PS (12:0/13:0) 43 pmol, PI
886 (12:0/13:0) 54 pmol, Cer (d18:1/25:0) 100 pmol, CE(19:0) 100 pmol, GlcCer (d18:1/12:0) 50 pmol, LacCer
887 (d18:1/12:0) 50 pmol, Sphinganine (d17:0) 50 pmol, Sphingosine-1-P (d17:1) 100 pmol, Sphingosine
888 (d17:1) 50 pmol, Galactosyl(ß) Sphingosine-d5 20 pmol, d5-TG ISTD Mix I 20 pmol, d5-DG ISTD Mix I 20
889 pmol, cholesterol (d7) 800 pmol.

890 ***Protein quantification***. Proteins were extracted form 20 µL of ammonium bicarbonate resuspended
891 fractions by adding 5 µL of lysis buffer (10% NP40, 2%SDS in PBS) and quantified by BCA protein assay kit
892 (ThermoFisher Scientific, 23225).

893 ***Lipid profiling data acquisition.*** Lipids extracts were diluted 1:5 with 95% mobile phase A (CH3CN:H2O
894 40:60; 5mM NH4COOCH3; 0.1% FA) plus 5% mobile phase B (IPA:H2O 90:10; 5mM NH4COOCH3; 0.1%
895 FA) and 1 µL injected on a liquid chromatography system nLC Ekspert nanoLC400 (Eksigent, 5033460C;
896 Singapore) coupled with a Triple TOF 6600 (AB Sciex; Singapore). Chromatography was performed using
897 an in house packed nanocolumn Kinetex EVO C18, 1.7 µm, 100 A, 0.75 x 100 mm. The gradient elution at
898 flow rate of 150 nL/min was initially started from 5 % of mobile phase B, linearly increased to 100 % B in
899 5 min, maintained for 45 min, then returned to the initial ratio in 2 min and maintained for 8 min.
900 Positive mode acquisition in MS was performed with the following parameters: mass over charge (m/z)

901 range 100–1700, T source 80C, Ion Spray Voltage 2000, Declustering Potential (DP) 80, fixed collision
902 energy 40 V (+). For IDA analysis (Top 8), range of m/z was set as 200–1800 in positive ion mode, target
903 ions were excluded for 20 sec after 2 occurrences (Analyst TF 1.7.1).
904 ***Data processing and analysis***. Lipidview workstation (version 1.3 beta, AB SCIEX, USA) was used for
905 lipids identification and quantitation. Lipid identification was based on exact mass, retention time, and
906 MS/MS pattern. Lipid species based on precursor fragment ion pairs were determined using a
907 comprehensive target list in LipidView (Sciex). Lipid species identification was performed using; the mass
908 tolerance of 0.05 in MS and 0.02 in MS/MS, s/n of 3 and % peak intensity > 0 for positive ion mode.
909 Lipid classes included for statistics and downstream analysis were: cholesterol ester (CE), sphingomyelin
910 (SM), diacylglycerol (DAG), triacylglycerol (TAG), ceramide (Cer) phosphatidylcholine (PC),
911 phosphatidylethanolamine (PE), phosphatidylglycerol (PG), phosphatidylinositol (PI), phosphatidylserine
912 (PS) and lysophosphatidylcholine (LPC), lysophosphatidylethanolamine (LPE), lysophosphatidylglycerol
913 (LPG), lysophosphatidylinositol (LPI), lysophosphatidylserine (LPS), hexosylceramide (HexCer),
914 dihexosylceramide (Hex2Cer), trihexosylceramide (Hex3Cer), sulphatides (SGalCer), ceramide-phosphate
915 (CerP), in positive mode.
916
917 **Statistics**
918 Data were analysed with Graph Pad Prism version 8 for Macintosh and expressed as the mean ± standard
919 error of the mean (SEM). The number of samples and the statistical tests and post-tests used are
920 specified in the legends to each figure. $p<0.05$ was considered statistically significant
921 For lipid analyses, statistical analysis was performed using Metaboanalyst 4.0 web tool
922 https://www.metaboanalyst.ca/MetaboAnalyst/faces/home.xhtml (Chong et al., 2018).
923

924 **References**

925 Allende, M.L., Cook, E.K., Larman, B.C., Nugent, A., Brady, J.M., Golebiowski, D., Sena-Esteves, M., Tifft,
926 C.J., and Proia, R.L. (2018). Cerebral organoids derived from Sandhoff disease-induced pluripotent
927 stem cells exhibit impaired neurodifferentiation. J. Lipid Res. *59*, 550-563.
928 Allewelt, H.B., Page, K., Taskindoust, M., Troy, J.D., Wood, S., Parikh, S., Prasad, V.K., and Kurtzberg, J.
929 (2016). Long-term functional outcomes following hematopoietic stem cell transplantation for krabbe
930 disease. Biol. Blood Marrow Transplant. *22*, S102–S103.
931 Ballabio, A., and Gieselmann, V. (2009). Lysosomal disorders: from storage to cellular damage. Biochim
932 Biophys Acta *1793*, 684–696.
933 Bayó-Puxan, N., Terrasso, A.P., Creyssels, S., Simão, D., Begon-Pescia, C., Lavigne, M., Salinas, S., Bernex,
934 F., Bosch, A., Kalatzis, V., et al. (2018). Lysosomal and network alterations in human
935 mucopolysaccharidosis type VII iPSC-derived neurons. Sci. Rep. *8*, 16644.
936 Berardi, A.S., Pannuzzo, G., Graziano, A., Costantino-Ceccarini, E., Piomboni, P., and Luddi, A. (2014).
937 Pharmacological chaperones increase residual beta-galactocerebrosidase activity in fibroblasts from
938 krabbe patients. Mol. Genet. Metab. *112*, 294–301.
939 Bieberich, E. (2012). It's a lipid's world: Bioactive lipid metabolism and signaling in neural stem cell
940 differentiation. Neurochem. Res. *37*,1208-1229.
941 Biffi, A., Montini, E., Lorioli, L., Cesani, M., Fumagalli, F., Plati, T., Baldoli, C., Martino, S., Calabria, A.,
942 Canale, S., et al. (2013). Lentiviral hematopoietic stem cell gene therapy benefits metachromatic
943 leukodystrophy. Science (80-.). *341*, 1233158.
944 Bongarzone, E.R. oque, Escolar, M.L. uisa, Gray, S.J. ames, Kafri, T., Vite, C.H. erman, and Sands, M.S.
945 teven (2016). Insights into the Pathogenesis and Treatment of Krabbe Disease. Pediatr. Endocrinol.
946 Rev. *13*, 689–696.
947 Borda, J.T., Alvarez, X., Mohan, M., Ratterree, M.S., Phillippi-Falkenstein, K., Lackner, A. a, and Bunnell, B.
948 a (2008). Clinical and immunopathologic alterations in rhesus macaques affected with globoid cell
949 leukodystrophy. Am J Pathol *172*, 98–111.
950 Bradbury, A.M., Rafi, M.A., Bagel, J.H., Brisson, B.K., Marshall, M.S., Pesayco Salvador, J., Jiang, X., Swain,
951 G.P., Prociuk, M.L., Odonnell, P.A., et al. (2018). AAVrh10 Gene Therapy Ameliorates Central and
952 Peripheral Nervous System Disease in Canine Globoid Cell Leukodystrophy (Krabbe Disease). Hum.
953 Gene Ther. *29,* 785-801.
954 Buratta, S., Urbanelli, L., Sagini, K., Giovagnoli, S., Caponi, S., Fioretto, D., Mitro, N., Caruso, D., and
955 Emiliani, C. (2017). Extracellular vesicles released by fibroblasts undergoing H-Ras induced senescence

956 show changes in lipid profile. PLoS One *12*, e0188840.
957 Canals, I., Soriano, J., Orlandi, J.G., Torrent, R., Richaud-Patin, Y., Jim??nez-Delgado, S., Merlin, S.,
958 Follenzi, A., Consiglio, A., Vilageliu, L., et al. (2015). Activity and high-order effective connectivity
959 alterations in sanfilippo C patient-specific neuronal networks. Stem Cell Reports *5*, 546–557.
960 Castelvetri, L.C., Givogri, M.I., Zhu, H., Smith, B., Lopez-Rosas, A., Qiu, X., van Breemen, R., and
961 Bongarzone, E.R. (2011). Axonopathy is a compounding factor in the pathogenesis of Krabbe disease.
962 Acta Neuropathol *122*, 35-48.
963 Chambers, S.M., Fasano, C.A., Papapetrou, E.P., Tomishima, M., Sadelain, M., and Studer, L. (2009).
964 Highly efficient neural conversion of human ES and iPS cells by dual inhibition of SMAD signaling. Nat.
965 Biotechnol. *27*, 275–280.
966 Chambers, S.M., Mica, Y., Studer, L., and Tomishima, M.J. (2011). Converting human pluripotent stem
967 cells to neural tissue and neurons to model neurodegeneration. Methods Mol. Biol. *793*, 87–97.
968 Chong, J., Soufan, O., Li, C., Caraus, I., Li, S., Bourque, G., Wishart, D.S., and Xia, J. (2018). MetaboAnalyst
969 4.0: Towards more transparent and integrative metabolomics analysis. Nucleic Acids Res. *46*, W486-
970 W494.
971 Claus, R., Dorer, M., Bunck, A., and Deigner, H. (2009). Inhibition of Sphingomyelin Hydrolysis: Targeting
972 the Lipid Mediator Ceramide as a Key Regulator of Cellular Fate. Curr. Med. Chem. *16*, 1978-2000.
973 Crowe, E.P., Tuzer, S.F., Cohen, J., Yetkin, E.C., D'Agostino, L., Sell, C., and Torres, C. (2016) Implications
974 of Cellular Senescence on Aging and Disease in the Brain. In: Rattan S., Hayflick L. (eds) Cellular Ageing
975 and Replicative Senescence. Healthy Ageing and Longevity. Springer, Cham
976 Duffner, P.K., Barczykowski, A., Jalal, K., Yan, L., Kay, D.M., and Carter, R.L. (2011). Early infantile Krabbe
977 disease: Results of the world-wide Krabbe registry. Pediatr. Neurol. *45*, 141–148.
978 Duffner, P.K., Barczykowski, A., Kay, D.M., Jalal, K., Yan, L., Abdelhalim, A., Gill, S., Gill, A.L., and Carter, R.
979 (2012). Later onset phenotypes of Krabbe disease: Results of the world-wide registry. Pediatr. Neurol.
980 *46*, 298–306.
981 Escolar, M.L., Kiely, B.T., Shawgo, E., Hong, X., Gelb, M.H., Orsini, J.J., Matern, D., and Poe, M.D. (2017).
982 Psychosine, a marker of Krabbe phenotype and treatment effect. Mol. Genet. Metab. *121*, 271-278.
983 Folch, J., Lees, M., and Sloane Stanley, G.H. (1957). A simple method for the isolation and purification of
984 total lipides from animal tissues. J. Biol. Chem. *226*, 497-509.
985 Folts, C.J., Scott-Hewitt, N., Pröschel, C., Mayer-Pröschel, M., and Noble, M. (2016). Lysosomal Re-
986 acidification Prevents Lysosphingolipid-Induced Lysosomal Impairment and Cellular Toxicity. PLoS
987 Biol. *14*.

988 Frati, G., Luciani, M., Meneghini, V., De Cicco, S., Ståhlman, M., Blomqvist, M., Grossi, S., Filocamo, M.,
989 Morena, F., Menegon, A., et al. (2018). Human iPSC-based models highlight defective glial and
990 neuronal differentiation from neural progenitor cells in metachromatic leukodystrophy. Cell Death
991 Dis. *9*, 698.
992 Gama Sosa, M.A., de Gasperi, R., Undevia, S., Yeretsian, J., Rouse 2nd, S.C., Lyerla, T.A., and Kolodny,
993 E.H. (1996). Correction of the galactocerebrosidase deficiency in globoid cell leukodystrophy-cultured
994 cells by SL3-3 retroviral-mediated gene transfer. Biochem Biophys Res Commun *218*, 766–771.
995 De Gasperi, R., Gama Sosa, M.A., Sartorato, E.L., Battistini, S., MacFarlane, H., Gusella, J.F., Krivit, W., and
996 Kolodny, E.H. (1996). Molecular heterogeneity of late-onset forms of globoid-cell leukodystrophy.
997 Am. J. Hum. Genet. *59*, 1233–1242.
998 De Gasperi, R., Gama Sosa, M.A., Sartorato, E., Battistini, S., Raghavan, S., and Kolodny, E.H. (1999).
999 Molecular basis of late-life globoid cell leukodystrophy. Hum Mutat *14*, 256–262.
1000 Gentner, B., Visigalli, I., Hiramatsu, H., Lechman, E., Ungari, S., Giustacchini, A., Schira, G., Amendola, M.,
1001 Quattrini, A., Martino, S., et al. (2010). Identification of hematopoietic stem cell-specific miRNAs
1002 enables gene therapy of globoid cell leukodystrophy. Sci. Transl. Med. *2*, 58ra84.
1003 Giri, S., Khan, M., Rattan, R., Singh, I., and Singh, A.K. (2006). Krabbe disease: psychosine-mediated
1004 activation of phospholipase A2 in oligodendrocyte cell death. J Lipid Res *47*, 1478–1492.
1005 Graziano, A.C.E., and Cardile, V. (2015). History, genetic, and recent advances on Krabbe disease. Gene.
1006 *555(1),* 2-13
1007 Del Grosso, A., Angella, L., Tonazzini, I., Moscardini, A., Giordano, N., Caleo, M., Rocchiccioli, S., and
1008 Cecchini, M. (2019). Dysregulated autophagy as a new aspect of the molecular pathogenesis of
1009 Krabbe disease. Neurobiol. Dis. *129*, 195-207.
1010 Gupta, A., Poe, M.D., Styner, M.A., Panigrahy, A., and Escolar, M.L. (2015). Regional differences in fiber
1011 tractography predict neurodevelopmental outcomes in neonates with infantile Krabbe disease.
1012 NeuroImage Clin. *7*, 792–798.
1013 Hannun, Y.A., and Obeid, L.M. (2002). The ceramide-centric universe of lipid-mediated cell regulation:
1014 Stress encounters of the lipid kind. J. Biol. Chem. *277*, 25847-25850.
1015 Hannun, Y.A., and Obeid, L.M. (2008). Principles of bioactive lipid signalling: Lessons from sphingolipids.
1016 Nat Rev Mol Cell Biol *9*, 139–150.
1017 Hannun, Y.A., and Obeid, L.M. (2017). Sphingolipids and their metabolism in physiology and disease. Nat.
1018 Rev. Mol. Cell Biol. *19*, 175-191.
1019 Hawkins-Salsbury, J. a, Parameswar, A.R., Jiang, X., Schlesinger, P.H., Bongarzone, E., Ory, D.S.,

1020 Demchenko, A. V, and Sands, M.S. (2013). Psychosine, the cytotoxic sphingolipid that accumulates in
1021 globoid cell leukodystrophy, alters membrane architecture. J. Lipid Res. *54*, 3303–3311.
1022 Hawkins-Salsbury, J.A., Shea, L., Jiang, X., Hunter, D.A., Guzman, A.M., Reddy, A.S., Qin, E.Y., Li, Y., Gray,
1023 S.J., Ory, D.S., et al. (2015). Mechanism-based combination treatment dramatically increases
1024 therapeutic efficacy in murine globoid cell leukodystrophy. J. Neurosci. *35*, 6495–6505.
1025 He, S., and Sharpless, N.E. (2017). Senescence in Health and Disease. Cell. *169*, 1000-1011.
1026 Higuchi, T., Kawagoe, S., Otsu, M., Shimada, Y., Kobayashi, H., Hirayama, R., Eto, K., Ida, H., Ohashi, T.,
1027 Nakauchi, H., et al. (2014). The generation of induced pluripotent stem cells (iPSCs) from patients
1028 with infantile and late-onset types of Pompe disease and the effects of treatment with acid-??-
1029 glucosidase in Pompe's iPSCs. Mol. Genet. Metab. *112*, 44–48.
1030 Huang, H.-P., Chuang, C.-Y., and Kuo, H.-C. (2012). Induced pluripotent stem cell technology for disease
1031 modeling and drug screening with emphasis on lysosomal storage diseases. Stem Cell Res. Ther. *3*, 34.
1032 Igisu, H., and Suzuki, K. (1984). Progressive accumulation of toxic metabolite in a genetic leukodystrophy.
1033 Science (80-.). *224*, 753–755.
1034 Irahara-Miyana, K., Otomo, T., Kondo, H., Hossain, M.A., Ozono, K., and Sakai, N. (2018). Unfolded
1035 protein response is activated in Krabbe disease in a manner dependent on the mutation type. J. Hum.
1036 Genet. *63*, 699–706.
1037 Jalal, K., Carter, R., Yan, L., Barczykowski, A., and Duffner, P.K. (2012). Does galactocerebrosidase activity
1038 predict krabbe phenotype? Pediatr. Neurol. *47*, 324–329.
1039 Jana, A., Hogan, E.L., and Pahan, K. (2009). Ceramide and neurodegeneration: Susceptibility of neurons
1040 and oligodendrocytes to cell damage and death. J. Neurol. Sci. *278*, 5-15.
1041 Jatana, M., Giri, S., and Singh, A.K. (2002). Apoptotic positive cells in Krabbe brain and induction of
1042 apoptosis in rat C6 glial cells by psychosine. Neurosci Lett *330*, 183–187.
1043 Kobolák, J., Molnár, K., Varga, E., Bock, I., Jezsó, B., Téglási, A., Zhou, S., Lo Giudice, M., Hoogeveen-
1044 Westerveld, M., Pijnappel, W.P., et al. (2019). Modelling the neuropathology of lysosomal storage
1045 disorders through disease-specific human induced pluripotent stem cells. Exp. Cell Res. *380*, 216-233.
1046 Lattanzi, A., Neri, M., Maderna, C., di Girolamo, I., Martino, S., Orlacchio, A., Amendola, M., Naldini, L.,
1047 and Gritti, A. (2010). Widespread enzymatic correction of CNS tissues by a single intracerebral
1048 injection of therapeutic lentiviral vector in leukodystrophy mouse models. Hum. Mol. Genet. *19*,
1049 2208–2227.
1050 Lattanzi, A., Salvagno, C., Maderna, C., Benedicenti, F., Morena, F., Kulik, W., Naldini, L., Montini, E.,
1051 Martino, S., and Gritti, A. (2014). Therapeutic benefit of lentiviral-mediated neonatal intracerebral

1052 gene therapy in a mouse model of globoid cell leukodystrophy. Hum. Mol. Genet. *23*, 3250–3268.
1053 Lee, S.J., Yi, T., Ahn, S.H., Lim, D.K., Hong, J.Y., Cho, Y.K., Lim, J., Song, S.U., and Kwon, S.W. (2014).
1054 Senescing human bone-marrow-derived clonal mesenchymal stem cells have altered
1055 lysophospholipid composition and functionality. J. Proteome Res. *13*, 1438-1449.
1056 Lee, W.C., Kang, D., Causevic, E., Herdt, A.R., Eckman, E.A., and Eckman, C.B. (2010). Molecular
1057 characterization of mutations that cause globoid cell leukodystrophy and pharmacological rescue
1058 using small molecule chemical chaperones. J Neurosci *30*, 5489–5497.
1059 Lemonnier, T., Blanchard, S., Toli, D., Roy, E., Bigou, S., Froissart, R., Rouvet, I., Vitry, S., Heard, J.M., and
1060 Bohl, D. (2011). Modeling neuronal defects associated with a lysosomal disorder using patient-
1061 derived induced pluripotent stem cells. Hum. Mol. Genet. *20*, 3653–3666.
1062 Lin, D., Fantz, C.R., Levy, B., Rafi, M.A., Vogler, C., Wenger, D.A., and Sands, M.S. (2005). AAV2/5 vector
1063 expressing galactocerebrosidase ameliorates CNS disease in the murine model of globoid-cell
1064 leukodystrophy more efficiently than AAV2. Mol Ther *12*, 422–430.
1065 Liu, J., Zhang, H., Li, Z., Hailemariam, T.K., Chakraborty, M., Jiang, K., Qiu, D., Bui, H.H., Peake, D.A., Kuo,
1066 M.S., et al. (2009). Sphingomyelin synthase 2 is one of the determinants for plasma and liver
1067 sphingomyelin levels in mice. Arterioscler. Thromb. Vasc. Biol. *29*, 850-856.
1068 Liu, Y., Gibson, J., Wheeler, J., Kwee, L.C., Santiago-Turla, C.M., Akafo, S.K., Lichter, P.R., Gaasterland,
1069 D.E., Moroi, S.E., Challa, P., et al. (2011). GALC deletions increase the risk of primary Open-Angle
1070 Glaucoma: The role of mendelian variants in complex disease. PLoS One. *6*, e27134.
1071 Lizardo, D.Y., Lin, Y.L., Gokcumen, O., and Atilla-Gokcumen, G.E. (2017). Regulation of lipids is central to
1072 replicative senescence. Mol. Biosyst. *13*, 498-509.
1073 Lizardo, D.Y., Parisi, L.R., Li, N., and Atilla-Gokcumen, G.E. (2018). Noncanonical Roles of Lipids in
1074 Different Cellular Fates. Biochemistry. *57*, 22-29.
1075 Lojewski, X., Staropoli, J.F., Biswas-Legrand, S., Simas, A.M., Haliw, L., Selig, M.K., Coppel, S.H., Goss, K.A.,
1076 Petcherski, A., Chandrachud, U., et al. (2014). Human iPSC models of neuronal ceroid lipofuscinosis
1077 capture distinct effects of TPP1 and CLN3 mutations on the endocytic pathway. Hum. Mol. Genet. *23*,
1078 2005–2022.
1079 Luni, C., Gagliano, O., and Elvassore, N. (2016). Microfluidic technology enhances the potential of human
1080 pluripotent stem cells. Biochem. Biophys. Res. Commun. *473*, 10–14.
1081 Luzi, P., Rafi, M.A., and Wenger, D.A. (1995). Characterization of the large deletion in the GALC gene
1082 found in patients with Krabbe disease. Hum. Mol. Genet. *4*, 2335–2338.
1083 Luzi, P., Rafi, M.A., Victoria, T., Baskin, G.B., and Wenger, D.A. (1997). Characterization of the rhesus

1084 monkey galactocerebrosidase (GALC) cDNA and gene and identification of the mutation causing
1085 globoid cell leukodystrophy (Krabbe disease) in this primate. Genomics *42*, 319–324.
1086 Maetzel, D., Sarkar, S., Wang, H., Abi-Mosleh, L., Xu, P., Cheng, A.W., Gao, Q., Mitalipova, M., and
1087 Jaenisch, R. (2014). Genetic and chemical correction of cholesterol accumulation and impaired
1088 autophagy in hepatic and neural cells derived from niemann-pick type C patient-specific iPS cells.
1089 Stem Cell Reports *2*, 866–880.
1090 Martino, S., Tiribuzi, R., Tortori, A., Conti, D., Visigalli, I., Lattanzi, A., Biffi, A., Gritti, A., and Orlacchio, A.
1091 (2009). Specific determination of beta-galactocerebrosidase activity via competitive inhibition of
1092 beta-galactosidase. Clin. Chem. *55*, 541–548.
1093 Meneghini, V., Lattanzi, A., Tiradani, L., Bravo, G., Morena, F., Sanvito, F., Calabria, A., Bringas, J., Fisher-
1094 Perkins, J.M., Dufour, J.P., et al. (2016). Pervasive supply of therapeutic lysosomal enzymes in the CNS
1095 of normal and Krabbe-affected non-human primates by intracerebral lentiviral gene therapy. EMBO
1096 Mol. Med. *8*, 489–510.
1097 Meneghini, V., Frati, G., Sala, D., De Cicco, S., Luciani, M., Cavazzin, C., Paulis, M., Mentzen, W., Morena,
1098 F., Giannelli, S., et al. (2017). Generation of Human Induced Pluripotent Stem Cell-Derived Bona Fide
1099 Neural Stem Cells for Ex Vivo Gene Therapy of Metachromatic Leukodystrophy. Stem Cells Transl.
1100 Med. *6*, 352–368.
1101 Misslin, C., Velasco-Estevez, M., Albert, M., O'Sullivan, S.A., and Dev, K.K. (2017). Phospholipase A2 is
1102 involved in galactosylsphingosine-induced astrocyte toxicity, neuronal damage and demyelination.
1103 PLoS One. *12*, e0187217.
1104 Mullen, T.D., Hannun, Y.A., Obeid, L.M., Hannun, Y.A., Obeid, L.M., Gatt, S., Gatt, S., Yavin, E., Gatt, S.,
1105 Sribney, M., et al. (2012). Ceramide synthases at the centre of sphingolipid metabolism and biology.
1106 Biochem. J. *441*, 139–150.
1107 Nicaise, A.M., Wagstaff, L.J., Willis, C.M., Paisie, C., Chandok, H., Robson, P., Fossati, V., Williams, A., and
1108 Crocker, S.J. (2019). Cellular senescence in progenitor cells contributes to diminished remyelination
1109 potential in progressive multiple sclerosis. Proc. Natl. Acad. Sci. U. S. A. *116*, 9030-9039.
1110 Ordoñez, M.P., and Steele, J.W. (2016). Modeling Niemann Pick type C1 using human embryonic and
1111 induced pluripotent stem cells. Brain Res. *1656*, 63-67.
1112 Panicker, L.M., Miller, D., Park, T.S., Patel, B., Azevedo, J.L., Awad, O., Masood, M.A., Veenstra, T.D.,
1113 Goldin, E., Stubblefield, B.K., et al. (2012). Induced pluripotent stem cell model recapitulates
1114 pathologic hallmarks of Gaucher disease. Proc. Natl. Acad. Sci. U. S. A. *109*, 18054–18059.
1115 Pellegrini, D., Del Grosso, A., Angella, L., Giordano, N., Dilillo, M., Tonazzini, I., Caleo, M., Cecchini, M.,

1116 and McDonnell, L.A. (2019). Quantitative microproteomics based characterization of the central and
1117 peripheral nervous system of a mouse model of Krabbe disease. Mol. Cell. Proteomics. *8*, 1227-1241.
1118 Potter, G.B., and Petryniak, M.A. (2016). Neuroimmune mechanisms in Krabbe's disease. J. Neurosci.
1119 Res. *94*, 1341-1348.
1120 Potter, G.B., Santos, M., Davisson, M.T., Rowitch, D.H., Marks, D.L., Bongarzone, E.R., and Petryniak, M.A.
1121 (2013). Missense mutation in mouse GALC mimics human gene defect and offers new insights into
1122 Krabbe disease. Hum Mol Genet *22*, 3397–3414.
1123 Rafi, M.A., Luzi, P., Chen, Y.Q., and Wenger, D.A. (1995). A large deletion together with a point mutation
1124 in the GALC gene is a common mutant allele in patients with infantile krabbe disease. Hum. Mol.
1125 Genet. *4*, 1285–1289.
1126 Rafi, M.A., Fugaro, J., Amini, S., Luzi, P., de Gala, G., Victoria, T., Dubell, C., Shahinfar, M., and Wenger,
1127 D.A. (1996). Retroviral vector-mediated transfer of the galactocerebrosidase (GALC) cDNA leads to
1128 overexpression and transfer of GALC activity to neighboring cells. Biochem Mol Med *58*, 142–150.
1129 Rafi, M.A., Rao, H.Z., Luzi, P., and Wenger, D.A. (2015). Long-term Improvements in Lifespan and
1130 Pathology in CNS and PNS After BMT Plus One Intravenous Injection of AAVrh10-GALC in Twitcher
1131 Mice. Mol. Ther. *23*, 1681–1690.
1132 Ribbens, J., Whiteley, G., Furuya, H., Southall, N., Hu, X., Marugan, J., Ferrer, M., and Maegawa, G.H.B.
1133 (2013). A high-throughput screening assay using Krabbe disease patient cells. Anal. Biochem. *434*, 15–
1134 25.
1135 Ricca, A., and Gritti, A. (2016). Perspective on innovative therapies for globoid cell leukodystrophy. J.
1136 Neurosci. Res. *94*, 1304–1317.
1137 Ricca, A., Rufo, N., Ungari, S., Morena, F., Martino, S., Kulik, W., Alberizzi, V., Bolino, A., Bianchi, F., Del
1138 Carro, U., et al. (2015). Combined gene/cell therapies provide long-term and pervasive rescue of
1139 multiple pathological symptoms in a murine model of globoid cell leukodystrophy. Hum. Mol. Genet.
1140 *24*, 3372–3389.
1141 Samie, M.A., and Xu, H. (2014). Lysosomal exocytosis and lipid storage disorders. J. Lipid Res. *55*, 995–
1142 1009.
1143 Santambrogio, S., Ricca, A., Maderna, C., Ieraci, A., Aureli, M., Sonnino, S., Kulik, W., Aimar, P., Bonfanti,
1144 L., Martino, S., et al. (2012). The galactocerebrosidase enzyme contributes to maintain a functional
1145 neurogenic niche during early post-natal CNS development. Hum. Mol. Genet. *21*, 4732–4750.
1146 Sessa, M., Lorioli, L., Fumagalli, F., Acquati, S., Redaelli, D., Baldoli, C., Canale, S., Lopez, I.D., Morena, F.,
1147 Calabria, A., et al. (2016). Lentiviral haemopoietic stem-cell gene therapy in early-onset

1148 metachromatic leukodystrophy: an ad-hoc analysis of a non-randomised, open-label, phase 1/2 trial.
1149 Lancet *388*, 476–487.
1150 Shi, Y., Inoue, H., Wu, J.C., and Yamanaka, S. (2017). Induced pluripotent stem cell technology: a decade
1151 of progress. Nat. Rev. Drug Discov. *16*, 115–130.
1152 Shin, D., Feltri, M.L., and Wrabetz, L. (2016). Altered Trafficking and Processing of GALC Mutants
1153 Correlates with Globoid Cell Leukodystrophy Severity. J. Neurosci. *36*, 1858–1870.
1154 Smith, B.R., Santos, M.B., Marshall, M.S., Cantuti-Castelvetri, L., Lopez-Rosas, A., Li, G., Van Breemen, R.,
1155 Claycomb, K.I., Gallea, J.I., Celej, M.S., et al. (2014). Neuronal inclusions of α-synuclein contribute to
1156 the pathogenesis of Krabbe disease. J. Pathol. *232*, 509–521.
1157 Son, M.-Y., Kwak, J.E., Seol, B., Lee, D.Y., Jeon, H., and Cho, Y.S. (2015). A novel human model of the
1158 neurodegenerative disease GM1 gangliosidosis using induced pluripotent stem cells demonstrates
1159 inflammasome activation. J. Pathol. *237*, 98-110.
1160 Spratley, S.J., Hill, C.H., Viuff, A.H., Edgar, J.R., Skjødt, K., and Deane, J.E. (2016). Molecular Mechanisms
1161 of Disease Pathogenesis Differ in Krabbe Disease Variants. Traffic *17*, 908–922.
1162 Sun, Y., Florer, J., Mayhew, C.N., Jia, Z., Zhao, Z., Xu, K., Ran, H., Liou, B., Zhang, W., Setchell, K.D.R., et al.
1163 (2015). Properties of neurons derived from induced pluripotent stem cells of Gaucher disease type 2
1164 patient fibroblasts: Potential role in neuropathology. PLoS One *10*.
1165 Suzuki, K. (1983). The twitcher mouse. A model of human globoid cell leukodystrophy (krabbe's disease).
1166 Am J Pathol *111*, 394–397.
1167 Suzuki, K., and Suzuki, Y. (1970). Globoid cell leucodystrophy (Krabbe's disease): deficiency of
1168 galactocerebroside beta-galactosidase. Proc Natl Acad Sci U S A *66*, 302–309.
1169 Tappino, B., Biancheri, R., Mort, M., Regis, S., Corsolini, F., Rossi, A., Stroppiano, M., Lualdi, S., Fiumara,
1170 A., Bembi, B., et al. (2010). Identification and characterization of 15 novel GALC gene mutations
1171 causing Krabbe disease. Hum. Mutat. *31*, E1894-1914.
1172 Teixeira, C.A., Miranda, C.O., Sousa, V.F., Santos, T.E., Malheiro, A.R., Solomon, M., Maegawa, G.H.,
1173 Brites, P., and Sousa, M.M. (2014). Early axonal loss accompanied by impaired endocytosis, abnormal
1174 axonal transport, and decreased microtubule stability occur in the model of Krabbe's disease.
1175 Neurobiol. Dis. *66*, 92–103.
1176 Tiscornia, G., Lorenzo Vivas, E., Matalonga, L., Berniakovich, I., Barragán Monasterio, M., Eguizábal, C.,
1177 Gort, L., González, F., Ortiz mellet, C., García Fernández, J.M., et al. (2013). Neuronopathic Gaucher's
1178 disease: Induced pluripotent stem cells for disease modelling and testing chaperone activity of small
1179 compounds. Hum. Mol. Genet. *22*, 633–645.

1180 Trayssac, M., Hannun, Y.A., and Obeid, L.M. (2018). Role of sphingolipids in senescence: Implication in
1181 aging and age-related diseases. J. Clin. Invest. *128*, 2702-2712.
1182 Trilck, M., Hübner, R., Seibler, P., Klein, C., Rolfs, A., and Frech, M.J. (2013). Niemann-Pick type C1
1183 patient-specific induced pluripotent stem cells display disease specific hallmarks. Orphanet J. Rare
1184 Dis. *8*, 144.
1185 Ungari, S., Montepeloso, A., Morena, F., Cocchiarella, F., Recchia, A., Martino, S., Gentner, B., Naldini, L.,
1186 and Biffi, A. (2015). Design of a regulated lentiviral vector for hematopoietic stem cell gene therapy of
1187 globoid cell leukodystrophy. Mol. Ther. Methods Clin. Dev. *2*, 15038.
1188 Vallejo-Diez, S., Fleischer, A., Martín-Fernández, J.M., Sánchez-Gilabert, A., and Bachiller, D. (2018).
1189 Generation of two induced pluripotent stem cells lines from a Mucopolysaccharydosis IIIB (MPSIIIB)
1190 patient. Stem Cell Res. *33*, 180-184.
1191 Venable, M.E., Lee, J.Y., Smyth, M.J., Bielawska, A., and Obeid, L.M. (1995). Role of ceramide in cellular
1192 senescence. J. Biol. Chem. *270*, 30701-30708.
1193 Wenger, D.A. (2000). Murine, canine and non-human primate models of Krabbe disease. Mol. Med.
1194 Today *6*, 449–451.
1195 Wenger, D.A., and Luzi, P. (2014). Krabbe Disease: Globoid Cell Leukodystrophy. In Rosenberg's
1196 Molecular and Genetic Basis of Neurological and Psychiatric Disease: Fifth Edition, pp. 337–346.
1197 White, A.B., Givogri, M.I., Lopez-Rosas, A., Cao, H., van Breemen, R., Thinakaran, G., and Bongarzone,
1198 E.R. (2009). Psychosine accumulates in membrane microdomains in the brain of krabbe patients,
1199 disrupting the raft architecture. J Neurosci *29*, 6068–6077.
1200 White, A.B., Galbiati, F., Givogri, M.I., Lopez Rosas, A., Qiu, X., Van Breemen, R., and Bongarzone, E.R.
1201 (2011). Persistence of psychosine in brain lipid rafts is a limiting factor in the therapeutic recovery of a
1202 mouse model for Krabbe disease. J. Neurosci. Res. *89*, 352–364.
1203 Yamanaka, S. (2007). Strategies and new developments in the generation of patient-specific pluripotent
1204 stem cells. Cell Stem Cell *1*, 39–49.
1205 Young, M.M., and Wang, H.G. (2018). Sphingolipids as Regulators of Autophagy and Endocytic
1206 Trafficking. Adv. Cancer Res. *140*, 27-60.
1207 Young, S.A., Mina, J.G., Denny, P.W., and Smith, T.K. (2012). Sphingolipid and ceramide homeostasis:
1208 Potential therapeutic targets. Biochem. Res. Int. *2012*, e248135.
1209 Yu, D., Swaroop, M., Wang, M., Baxa, U., Yang, R., Yan, Y., Coksaygan, T., DeTolla, L., Marugan, J.J.,
1210 Austin, C.P., et al. (2014). Niemann-Pick Disease Type C: Induced Pluripotent Stem Cell-Derived
1211 Neuronal Cells for Modeling Neural Disease and Evaluating Drug Efficacy. J. Biomol. Screen. *19*, 1164–

1212 1173.

1213 Zhang, P., Kishimoto, Y., Grammatikakis, I., Gottimukkala, K., Cutler, R.G., Zhang, S., Abdelmohsen, K.,
1214 Bohr, V.A., Misra Sen, J., Gorospe, M., et al. (2019). Senolytic therapy alleviates Aβ-associated
1215 oligodendrocyte progenitor cell senescence and cognitive deficits in an Alzheimer's disease model.
1216 Nat. Neurosci. *22*, 719-728.

Figure 1

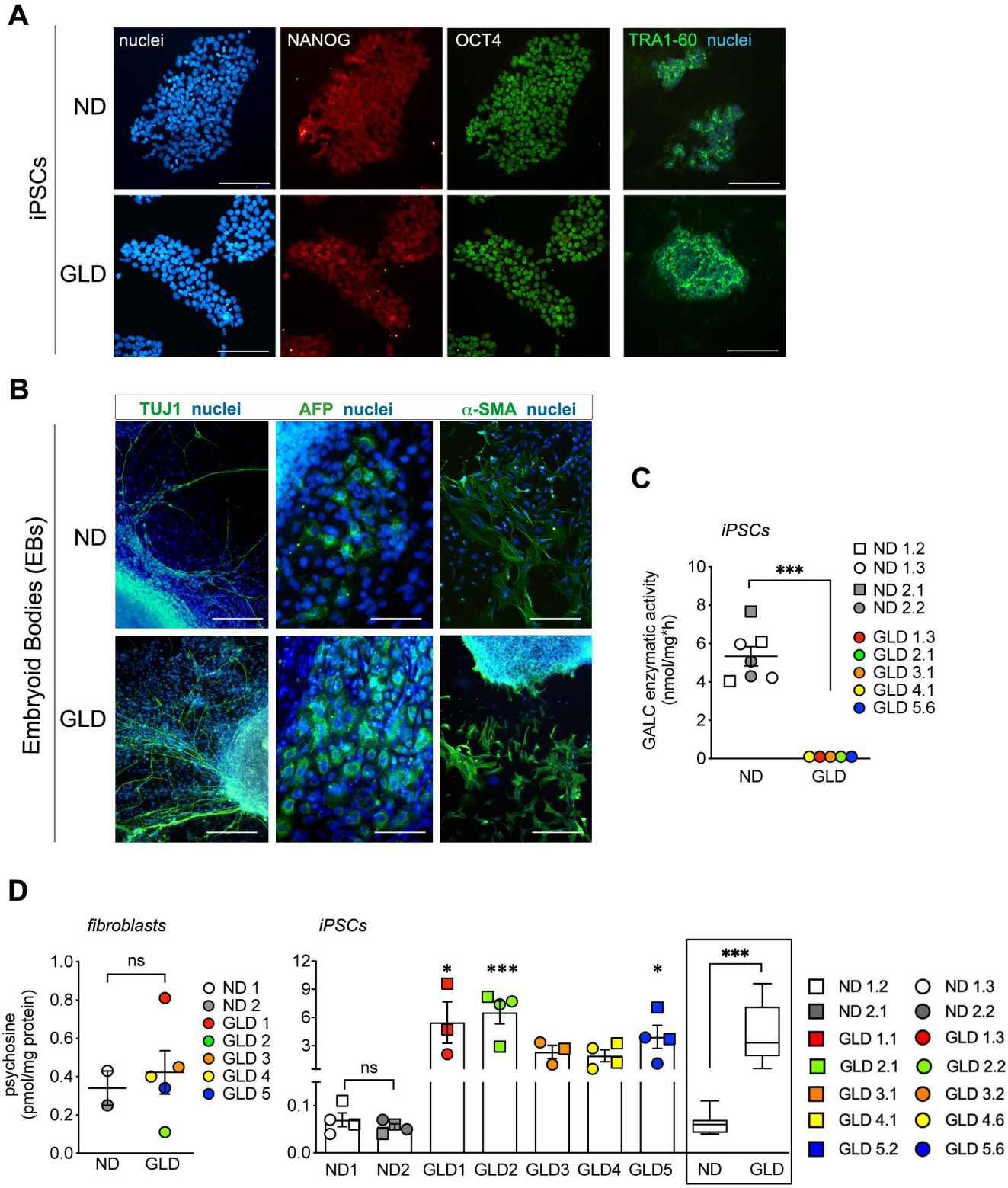
A
iPSCs
ND
GLD
nuclei
NANOG
OCT4
TRA1-60 nuclei
B
Embryoid Bodies (EBs)
ND
GLD
TUJ1 nuclei
AFP nuclei
α-SMA nuclei
C
iPSCs
GALC enzymatic activity (nmol/mg*h)
***
ND
GLD
ND 1.2
ND 1.3
ND 2.1
ND 2.2
GLD 1.3
GLD 2.1
GLD 3.1
GLD 4.1
GLD 5.6
D
fibroblasts
iPSCs
psychosine (pmol/mg protein)
ns
ND 1
ND 2
GLD 1
GLD 2
GLD 3
GLD 4
GLD 5
ND1
ND2
GLD1
GLD2
GLD3
GLD4
GLD5
ND 1.2
ND 1.3
ND 2.1
ND 2.2
GLD 1.1
GLD 1.3
GLD 2.1
GLD 2.2
GLD 3.1
GLD 3.2
GLD 4.1
GLD 4.6
GLD 5.2
GLD 5.6

Figure 2

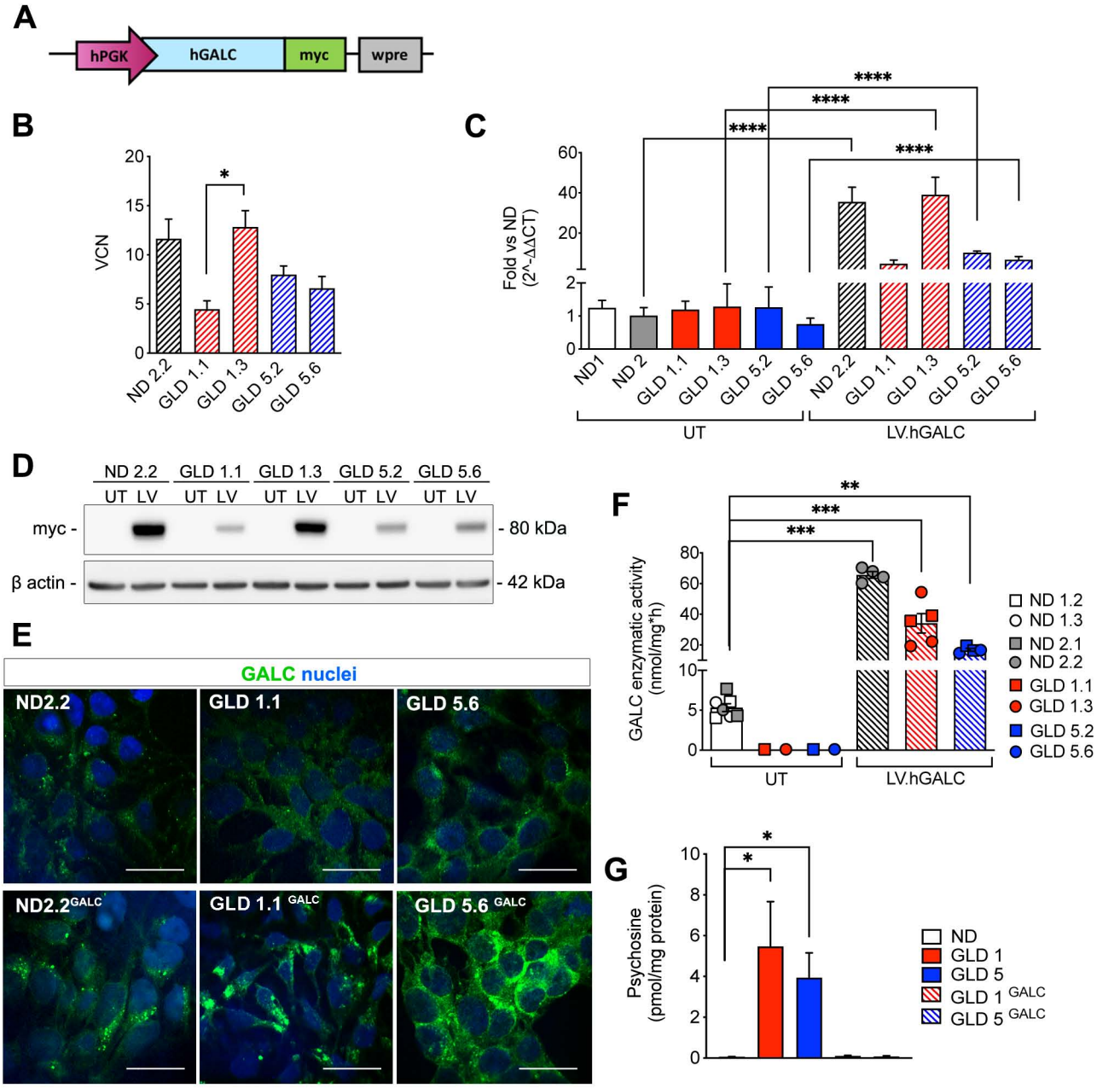
A
hPGK
hGALC
myc
wpre
B
VCN
ND 2.2
GLD 1.1
GLD 1.3
GLD 5.2
GLD 5.6
C
Fold vs ND (2^-ΔΔCT)
ND1
ND 2
UT
LV.hGALC
D
ND 2.2
GLD 1.1
GLD 1.3
GLD 5.2
GLD 5.6
UT LV
myc -
β actin -
- 80 kDa
- 42 kDa
E
GALC nuclei
ND2.2
GLD 1.1
GLD 5.6
ND2.2GALC
GLD 1.1 GALC
GLD 5.6 GALC
F
GALC enzymatic activity (nmol/mg*h)
ND 1.2
ND 1.3
ND 2.1
ND 2.2
GLD 1.1
GLD 1.3
GLD 5.2
GLD 5.6
G
Psychosine (pmol/mg protein)
ND
GLD 1
GLD 5
GLD 1 GALC
GLD 5 GALC

Figure 3

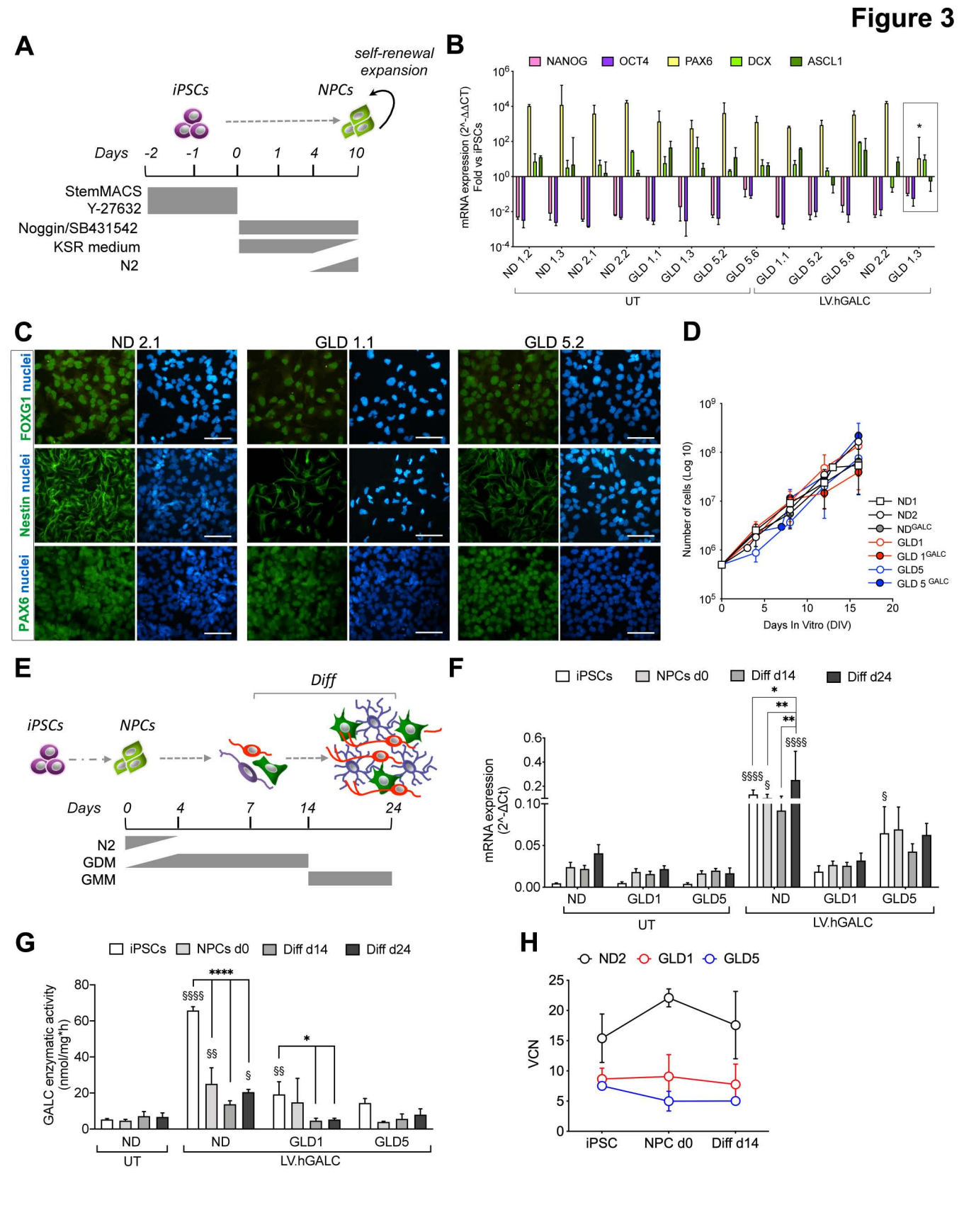
A
self-renewal expansion
iPSCs
NPCs
Days -2 -1 0 1 4 10
StemMACS
Y-27632
Noggin/SB431542
KSR medium
N2
B
NANOG
OCT4
PAX6
DCX
ASCL1
mRNA expression (2^-ΔΔCT) Fold vs iPSCs
ND 1.2
ND 1.3
ND 2.1
ND 2.2
GLD 1.1
GLD 1.3
GLD 5.2
GLD 5.6
GLD 1.1
GLD 5.2
GLD 5.6
ND 2.2
GLD 1.3
UT
LV.hGALC
C
ND 2.1
GLD 1.1
GLD 5.2
FOXG1 nuclei
Nestin nuclei
PAX6 nuclei
D
Number of cells (Log 10)
Days In Vitro (DIV)
ND1
ND2
ND GALC
GLD1
GLD 1 GALC
GLD5
GLD 5 GALC
E
Diff
iPSCs
NPCs
Days 0 4 7 14 24
N2
GDM
GMM
F
iPSCs
NPCs d0
Diff d14
Diff d24
mRNA expression (2^-ΔCt)
ND
GLD1
GLD5
UT
LV.hGALC
G
iPSCs
NPCs d0
Diff d14
Diff d24
GALC enzymatic activity (nmol/mg*h)
ND
GLD1
GLD5
UT
LV.hGALC
H
ND2
GLD1
GLD5
VCN
iPSC
NPC d0
Diff d14

Figure 4

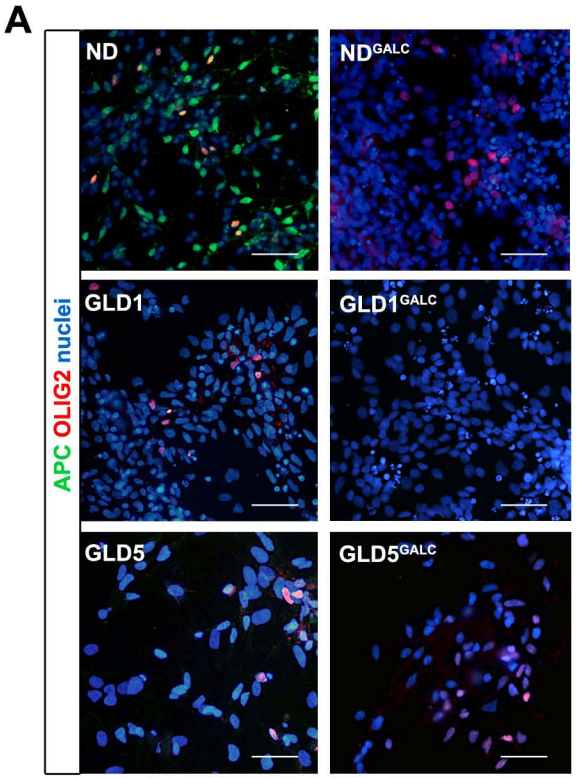
A
ND
ND^GALC
GLD1
GLD1^GALC
GLD5
GLD5^GALC
APC OLIG2 nuclei

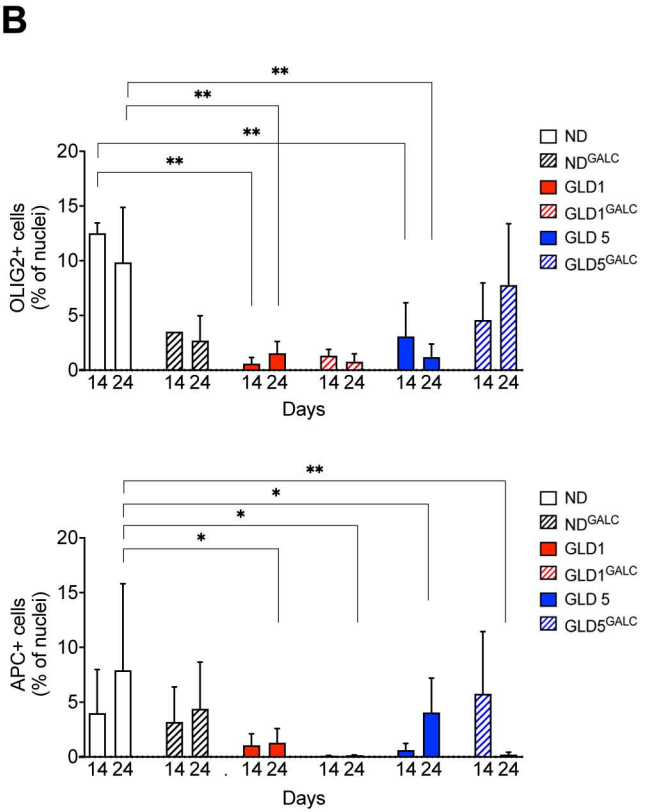
B
OLIG2+ cells (% of nuclei)
Days
14 24
ND
ND^GALC
GLD1
GLD1^GALC
GLD 5
GLD5^GALC
APC+ cells (% of nuclei)

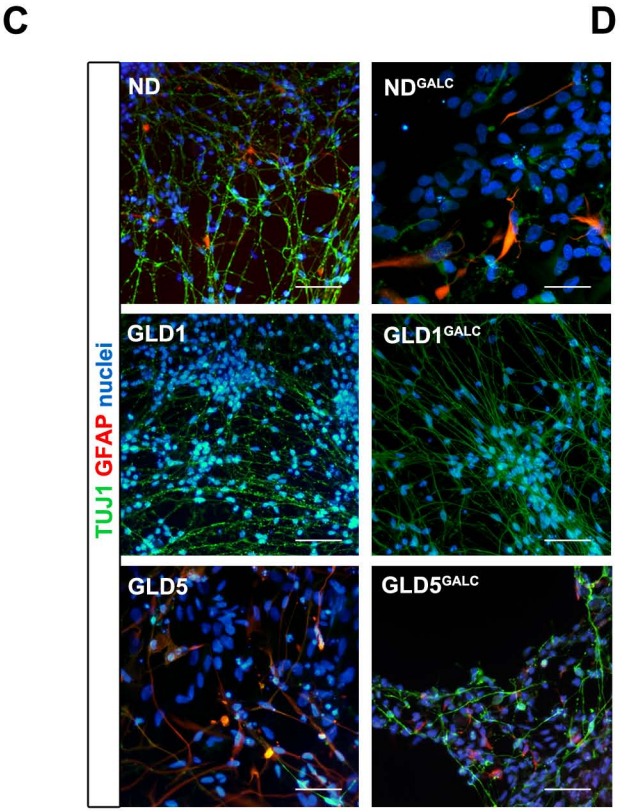
C
ND
ND^GALC
GLD1
GLD1^GALC
GLD5
GLD5^GALC
TUJ1 GFAP nuclei

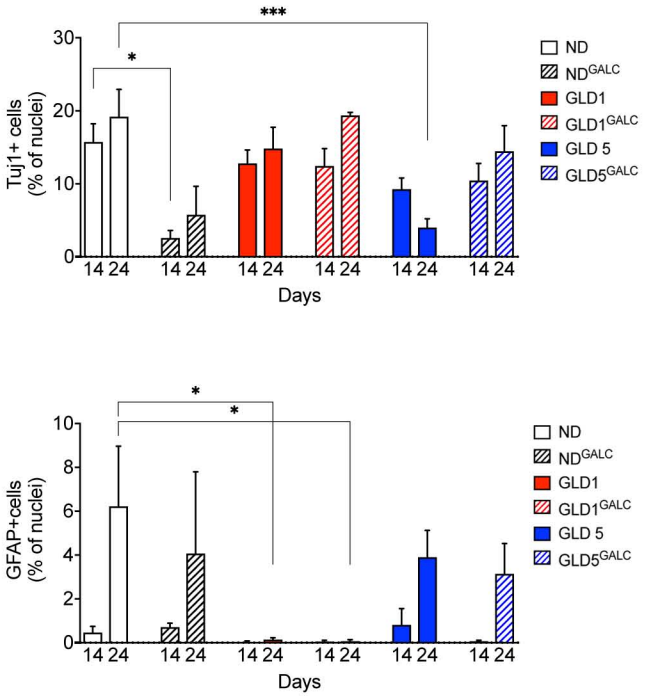
D
Tuj1+ cells (% of nuclei)
GFAP+cells (% of nuclei)
Days
14 24
ND
ND^GALC
GLD1
GLD1^GALC
GLD 5
GLD5^GALC

Figure 5

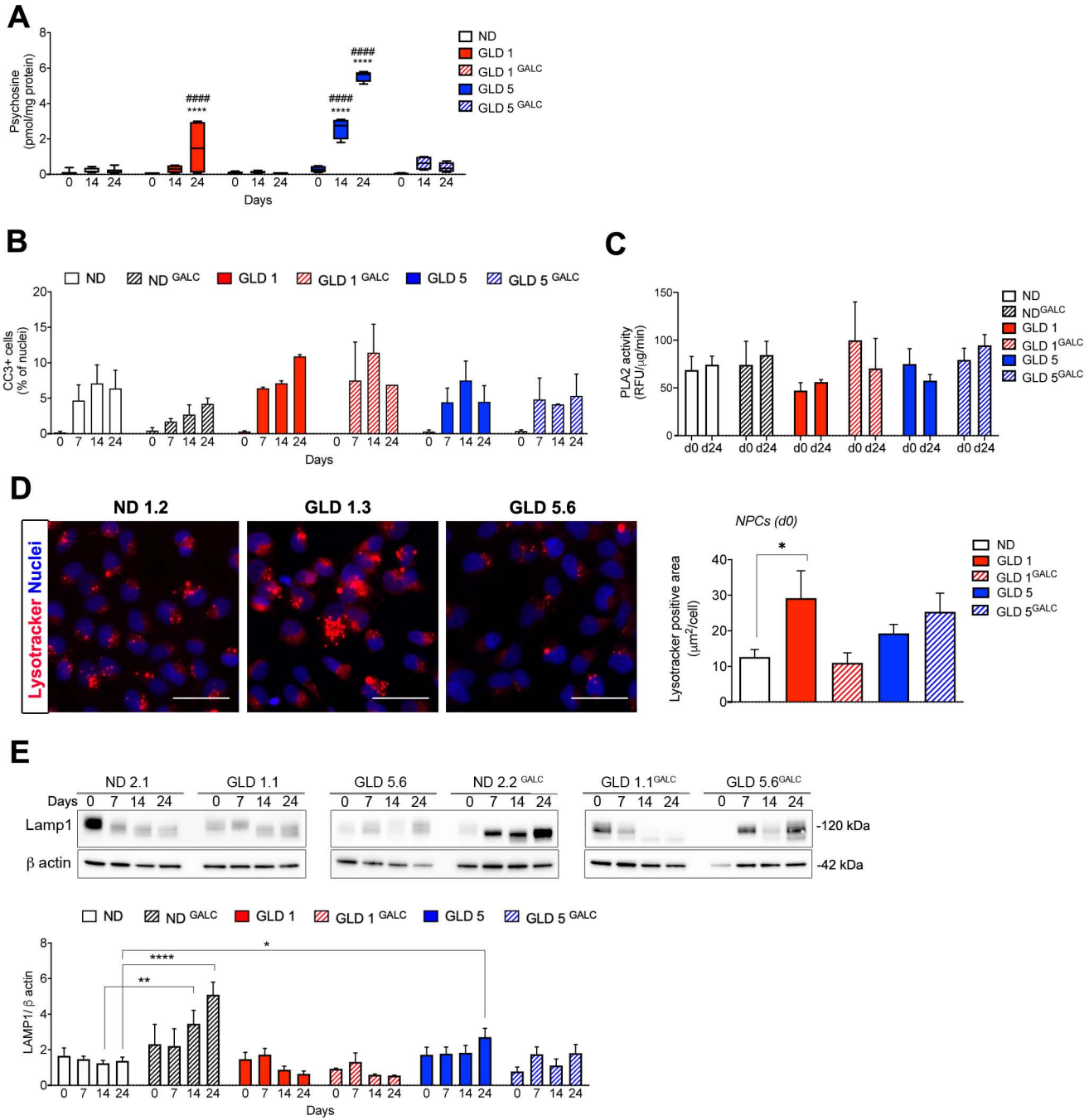
A
Psychosine (pmol/mg protein)
Days
ND
GLD 1
GLD 1 GALC
GLD 5
GLD 5 GALC
B
CC3+ cells (% of nuclei)
Days
C
PLA2 activity (RFU/µg/min)
d0 d24
D
ND 1.2
GLD 1.3
GLD 5.6
Lysotracker Nuclei
NPCs (d0)
Lysotracker positive area (µm²/cell)
E
ND 2.1
GLD 1.1
GLD 5.6
ND 2.2 GALC
GLD 1.1 GALC
GLD 5.6 GALC
Days
Lamp1
β actin
-120 kDa
-42 kDa
LAMP1/ β actin

Figure 6

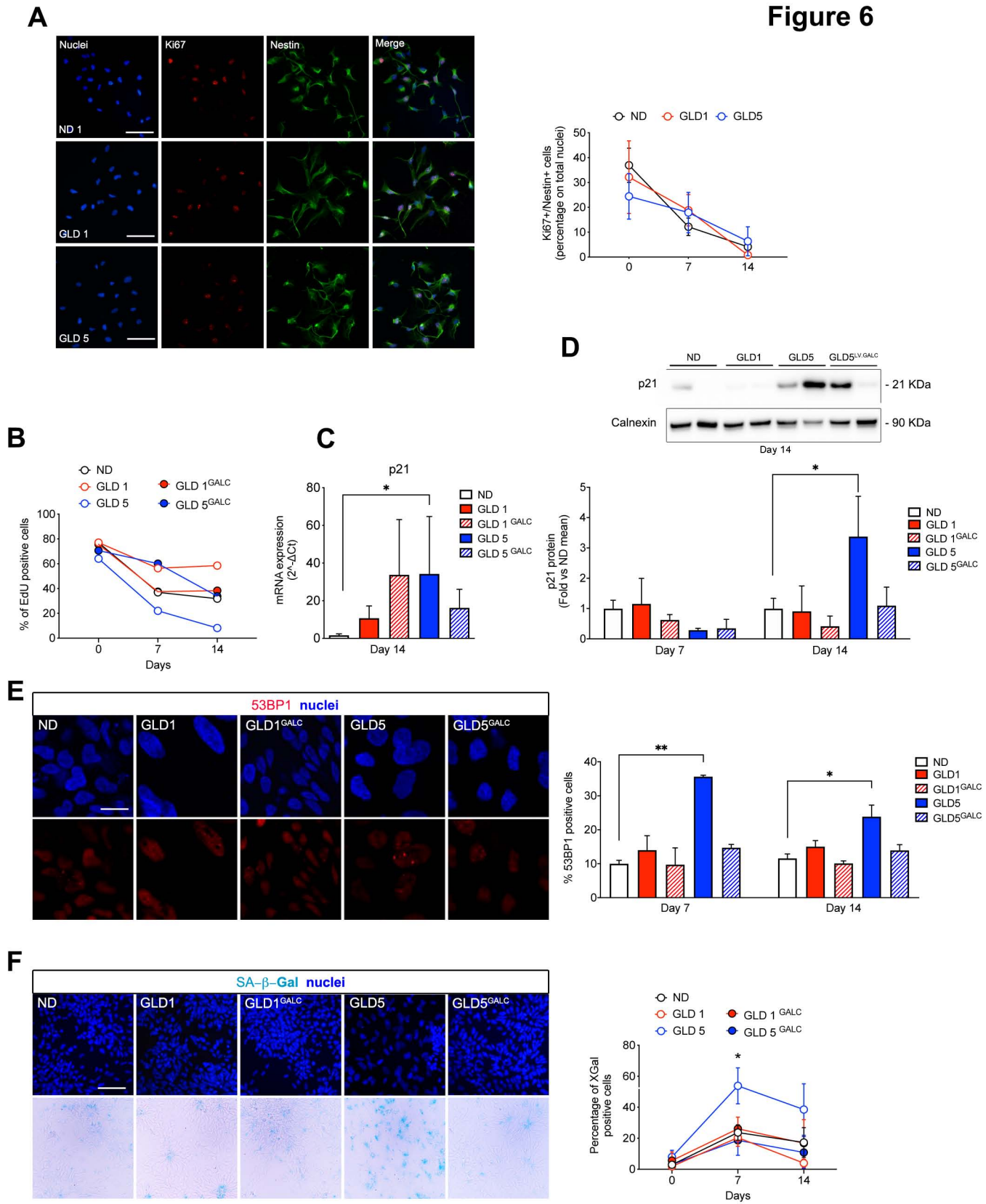
A
Nuclei
Ki67
Nestin
Merge
ND 1
GLD 1
GLD 5
ND
GLD1
GLD5
Ki67+/Nestin+ cells (percentage on total nuclei)
0
7
14
B
ND
GLD 1
GLD 5
GLD 1GALC
GLD 5GALC
% of EdU positive cells
Days
C
p21
mRNA expression (2^-ΔCt)
Day 14
D
ND
GLD1
GLD5
GLD5LV.GALC
p21
Calnexin
- 21 KDa
- 90 KDa
Day 14
p21 protein (Fold vs ND mean)
Day 7
Day 14
E
53BP1 nuclei
ND
GLD1
GLD1GALC
GLD5
GLD5GALC
% 53BP1 positive cells
Day 7
Day 14
F
SA-β-Gal nuclei
Percentage of XGal positive cells
Days

Figure 7

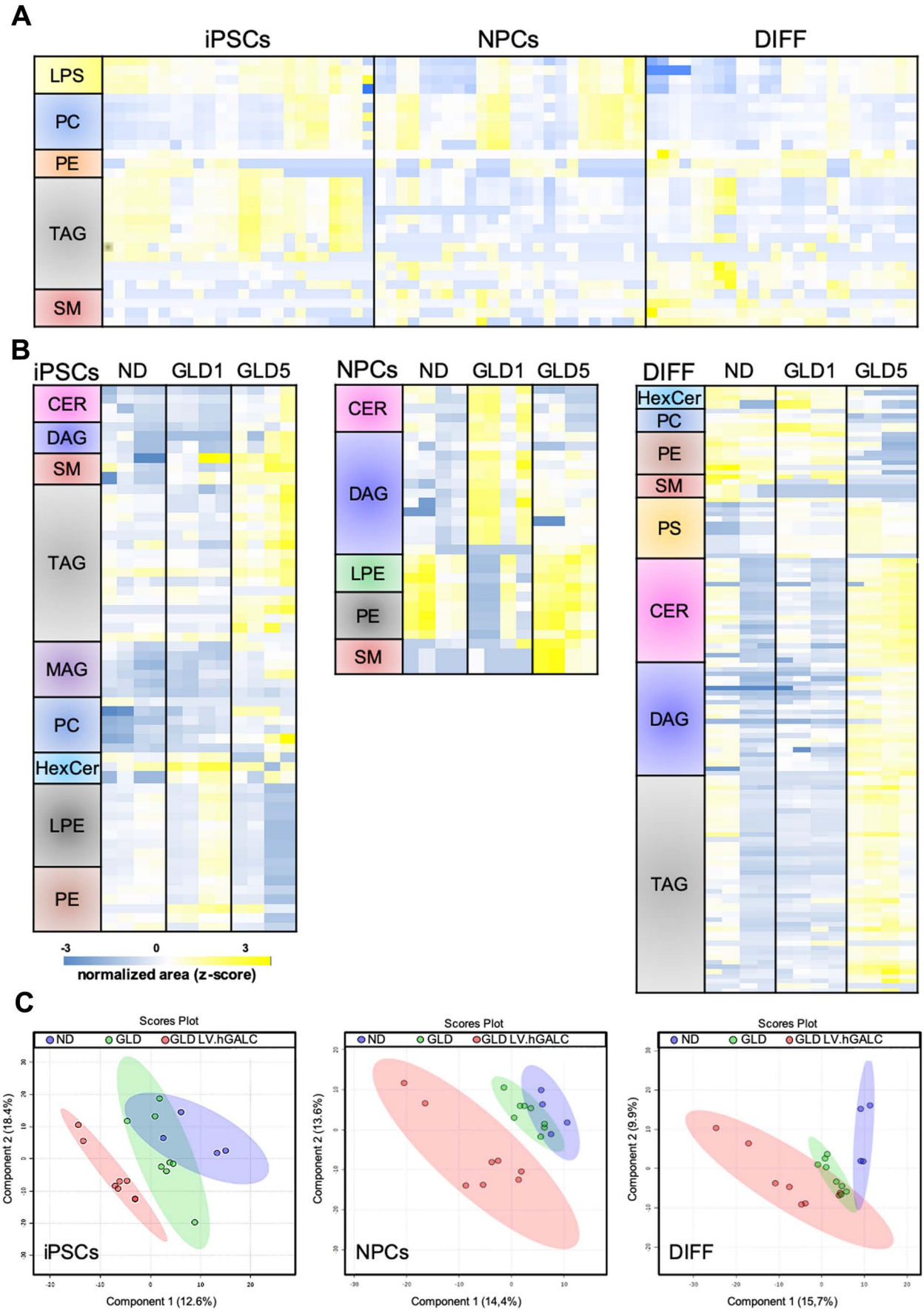
A
iPSCs
NPCs
DIFF
LPS
PC
PE
TAG
SM
B
iPSCs ND GLD1 GLD5
CER
DAG
SM
TAG
MAG
PC
HexCer
LPE
PE
NPCs ND GLD1 GLD5
CER
DAG
LPE
PE
SM
DIFF ND GLD1 GLD5
HexCer
PC
PE
SM
PS
CER
DAG
TAG
-3
0
3
normalized area (z-score)
C
Scores Plot
ND
GLD
GLD LV.hGALC
Component 2 (18.4%)
Component 1 (12.6%)
iPSCs
Scores Plot
ND
GLD
GLD LV.hGALC
Component 2 (13.6%)
Component 1 (14,4%)
NPCs
Scores Plot
ND
GLD
GLD LV.hGALC
Component 2 (9.9%)
Component 1 (15,7%)
DIFF